

**THESIS TO OBTAIN THE DEGREE OF DOCTOR
OF THE UNIVERSITY OF MONTPELLIER**

In SyAM - Automatic and Microelectronic Systems

Doctoral school: Information, Structures, and Systems sciences

Research Unit: LIRMM

Body biasing fault injection: modeling

Presented by Geoffrey Chancel

COMPILATION DATE: 2023-08-22 18:04:29+02:00

Under the supervision of TO BE COMPLETED

Thesis Committee:

Philippe Maurine , Associate Professor ?? , University of Montpellier

Thesis Director

Jean-Marc Gallière, Associate Professor ?? , University of Montpellier

Thesis Supervisor



**UNIVERSITÉ DE
MONTPELLIER**

Abstract [2023-08-22 18:04:29+02:00](#)

Résumé de la thèse [2023-08-22 18:04:29+02:00](#)

Acknowledgements 2023-08-22 18:04:29+02:00

The authors acknowledge the support of the French Agence Nationale de la Recherche (ANR), under grant ANR-19-CE39-0008 (project ARCHI-SEC). They also acknowledge the French Ministère des Armées – Agence de l’innovation de défense (AID) under grant ID-UM-2019 65 0036.

Contents

List of Figures	ix	
List of Tables	xi	
List of algorithms JAAJ	xiii	
List of Acronyms	xv	
Publications	xvi	
General introduction	xvii	
1 Introduction and state of the art	2023-08-22 18:04:19+02:00	1
1.1 Summary	2023-08-22 18:04:19+02:00	2
1.2 Introduction	2023-08-22 18:04:19+02:00	2
1.3 Side-channel attacks	2023-08-22 18:04:19+02:00	6
1.3.1 Timing attacks	2023-08-22 18:04:19+02:00	6
1.3.2 Power analysis and electromagnetic analysis attacks	2023-08-22 18:04:19+02:00	6
1.4 Fault-injection attacks	2023-08-22 18:04:19+02:00	8
2 Body Biasing Injection platforms and good practices	2023-08-22 18:04:19+02:00	9
2.1 Summary	2023-08-22 18:04:19+02:00	10
2.2 Introduction	2023-08-22 18:04:19+02:00	10
2.2.1 Platform equipment	2023-08-22 18:04:19+02:00	10
2.2.2 The hardware	2023-08-22 18:04:19+02:00	10
2.2.3 The software	2023-08-22 18:04:19+02:00	13
2.3 Body Biasing Injection enhanced practice	2023-08-22 18:04:19+02:00	14
2.3.1 BBI practice in the state of the art	2023-08-22 18:04:19+02:00	14
2.3.2 Enhanced BBI practice	2023-08-22 18:04:19+02:00	17

2.3.3	BBI practices: a simple actual comparisons	2023-08-22 18:04:19+02:00	18
2.4	Giraud's differential fault attack	2023-08-22 18:04:19+02:00	20
2.5	Conclusion	2023-08-22 18:04:19+02:00	22
3	Integrated circuits modeling	2023-08-22 18:04:19+02:00	25
3.1	Summary	2023-08-22 18:04:19+02:00	26
3.2	Introduction	2023-08-22 18:04:19+02:00	26
3.3	Electrical models	2023-08-22 18:04:19+02:00	27
3.3.1	Standard-cell segment models	2023-08-22 18:04:19+02:00	31
3.4	Preliminary model validation	2023-08-22 18:04:19+02:00	35
3.5	Voltage pulse generator model and further validation	2023-08-22 18:04:19+02:00	37
3.5.1	Early generator models	2023-08-22 18:04:19+02:00	37
3.5.2	Further generator models and verification	2023-08-22 18:04:19+02:00	38
3.6	Experimental comparisons	2023-08-22 18:04:19+02:00	39
3.7	Conclusion	2023-08-22 18:04:19+02:00	39
4	Substrate thinning analysis	2023-08-22 18:04:19+02:00	43
4.1	Summary	2023-08-22 18:04:19+02:00	44
4.2	Introduction	2023-08-22 18:04:19+02:00	44
4.3	Geometric and electrical modeling	2023-08-22 18:04:19+02:00	45
4.3.1	Geometric modeling	2023-08-22 18:04:19+02:00	45
4.3.2	Electrical approach	2023-08-22 18:04:19+02:00	49
4.4	Models validation	2023-08-22 18:04:19+02:00	51
4.4.1	IC substrate thinning quick look	2023-08-22 18:04:19+02:00	51
4.4.2	Experiments with thinned circuits	2023-08-22 18:04:19+02:00	52
4.5	Conclusion	2023-08-22 18:04:19+02:00	54
5	Fault model	2023-08-22 18:04:19+02:00	55
5.1	Summary	2023-08-22 18:04:19+02:00	56
5.2	Introduction	2023-08-22 18:04:19+02:00	56
5.3	Charge extortion	2023-08-22 18:04:19+02:00	57
5.3.1	Sequential logic operation and simple fault model	2023-08-22 18:04:19+02:00	57
5.3.2	Charge extortion	2023-08-22 18:04:19+02:00	58
5.4	Silicon substrate charges propagation	2023-08-22 18:04:19+02:00	58

5.5 Logic gates simulation under BBI 2023-08-22 18:04:19+02:00	58
6 Conclusion	59
Bibliography	61

List of Figures

2.1	Dual-well and triple-well inverter silicon sectional view	11
2.2	ChipSHOUTER®-PicoEMP from NewAE Technology Inc.	11
2.3	Front side of the Avtech Electrosystems Ltd. AVRK-4-B High Voltage Pulser	12
2.4	BBI platform example in the state of the art: schematic	14
2.5	BBI platform example in the state of the art: simulation	15
2.6	The proposed enhanced BBI platform	17
2.7	BBI enhancements with actual measurements	18
2.8	Fault analysis mapping	20
3.1	Dual-well and triple-well inverter silicon sectional view	28
3.2	Surface subdivision improvement.	29
3.3	Three-dimensional Dual-Well and Triple-Well IC comprehensive standard-cell electrical schematic.	30
3.4	Elementary substrate 3D netlist	33
3.5	Elementary substrate SPICE netlist	33
3.6	SCS substrate layer SPICE netlist	33
3.7	Three-dimensional standard-cell segments interconnection example.	35
3.8	Mixed substrates operating point.	36
3.9	Dual-well and triple-well cross-sectional current distribution view at the apex of the voltage pulse	38
4.1	BBI susceptibility area cross-sectional 2D view	46
4.2	Simulated non-thinned IC (140 µm) substrate voltage distribution: peak of the first voltage pulse edge	49
4.3	Simulated thinned IC (60 µm) substrate voltage distribution: peak of the first voltage pulse edge	50

4.4	Fault susceptibility maps	52
4.5	Susceptibility area spreading	52
4.6	Fault susceptibility maps couples	52
5.1	Sequential logic operation and BBI sampling fault susceptibility	57

List of Tables

2.1	FAM faults description	21
2.2	Giraud's DFA results	22
3.1	Dual-well, triple-well and mixed substrates SCS operating point.	36

List of Algorithms

1	Integrated circuit SPICE netlist generation algorithm.	41
---	--	----

List of Acronyms

BBI	Body Biasing Injection
BSIM	Berkeley Short-channel IGFET Model
DPA	Differential Power Analysis
ECC	Elliptic-Curve Cryptography
EMFI	Electro-Magnetic Fault Injection
FAM	Fault Analysis Mapping
FIB	Focused Ion Beam
FSM	Fault Susceptibility Map
LFI	Laser Fault Injection
PCC	Pearson Correlation Coefficient
RAM	Random Access Memory
SCA	Side Channel Attack
SCS	Standard Cell Segment
SPA	Simple Power Analysis

Publications 2023-08-22 18:04:29+02:00

- [1]

General introduction

2023-08-22 18:04:29+02:00

Over the past twelve years, various fault injection methods have been extensively studied. The most noteworthy were Electromagnetic Fault Injection (EMFI) and Laser Fault Injection (LFI). Indeed, among all studies, elaborated models have been proposed to study and predict the effects of EMFI on integrated circuits (IC), and IC substrate thinning effects have been studied concerning LFI efficiency. However, Body Biasing Injection (BBI), although introduced in 2011, has been less documented than the above injection methods. Within this context, this work aims at tackling the interests of this technique over others, replacing them or

The **first** chapter of this manuscript presents the global fault injection and specific Body Biasing Injection state of the art, mainly concerning side-channel attacks. Various fault injection platforms are presented, ranging from electromagnetic fault injection to laser-fault injection, eventually introducing body-biasing injection.

Then, the **second** chapter introduces new enhanced practices for body biasing injection. It aims at presenting the work concerning various improvements for the practice of BBI. These contributions aim, thanks to minor modifications and improvements of existing platforms, at improving body biasing injection efficiency.

Afterward, the **third** chapter focuses on IC modeling specifically for the practice of BBI. It introduces electrical models and algorithms allowing to generate and simulate integrated circuits in a BBI context. The introduced models have the advantage to offer simulation duration on a human timescale, thus allowing to evaluate and study large circuits in short amount of time.

Subsequently, the **fourth** discusses a common practice when performing fault injec-

tion: the thinning of integrated circuits' substrate. This topic has been addressed extensively concerning laser fault injection, and we present our contribution concerning BBI. It mainly relates to studying IC behavioral differences and BBI efficiency. Various models are proposed in order to get different approaches of the subject, allowing to predict differently electrical and physical phenomena. Mathematical models are also derived from the previous models, allowing to calculate optimal experimental parameters in addition to predicting circuit behavior.

Eventually, the **fifth and last** chapter introduces a fault model, allowing to explain at a circuit level and at a transistor level how faults are created under body biasing injection.

I

Introduction and state of the art 2023-08-22

18:04:29+02:00

chap:1_stateOfTheArt

Contents

1.1	Summary <small>2023-08-22 18:04:19+02:00</small>	2
1.2	Introduction <small>2023-08-22 18:04:19+02:00</small>	2
1.3	Side-channel attacks <small>2023-08-22 18:04:19+02:00</small>	6
1.3.1	Timing attacks <small>2023-08-22 18:04:19+02:00</small>	6
1.3.2	Power analysis and electromagnetic analysis attacks <small>2023-08-22 18:04:19+02:00</small>	6
1.4	Fault-injection attacks <small>2023-08-22 18:04:19+02:00</small>	8

1.1 Summary 2023-08-22 18:04:29+02:00

chap:1;sect:summary

This chapter reviews the state-of-the-art concerning fault injection methods. It first defines the interest of studying fault injection and its context. Then, various fault injection techniques are presented and their differences, advantages and disadvantages are analyzed. Specifically, platforms equipment across all methods is described alongside the different techniques employed to perform such fault injection. Eventually, the current work topic is introduced.

1.2 Introduction 2023-08-22 18:04:29+02:00

chap:1;sect:intro

In our time, almost every business sector and every part of our surroundings, directly or indirectly, use integrated electronics circuits. It ranges from smart-cards to super-computers, through military devices, cell-phones, Cyber-Physical Systems (CPS) and Internet-of-Things (IoT) objects to name but a few.

Traditionally, integrated circuits design mainly focused on performance upgrades over the generations. Performance was measured thanks to two factors: computation speed and silicon surface. Within this context, power consumption was not a design constraint, therefore, integrated circuits became more and more energy-consuming. However, with the advent of portable devices, power consumption became a predominant design factor over speed, and space and got included into the former design flows. Nevertheless, less space and more speed does not physically equate with less energy. Alongside, new systems have emerged and have massively grown these past decades: IoT and CPS. On one hand, CPS are often systems where hardware and software are interlaced and thought together, and can be drastically different from one application to another. On the other hand, IoT systems have often less coordination between hardware and software, but are commonly more flexible. Whatever, both of these systems have something strong in common: their security is fundamental. Therefore, in this context, as it has been proposed in [2], and because security had been adopted as a countermeasure after the design flow, it has to enter as a fourth design rule when creating integrated circuits. This is required because a secure system has to

ensure that every data going in and out of it are subject to the following criteria:

- Authenticity: data received have to come from the sender
- Integrity: data cannot be altered in any way
- Confidentiality: data cannot be accessed (read or written) by third-parties

Therefore, it is imperative to study and comprehend the strategies for enhancing IC security in order to develop future integrated circuits that are designed with security in mind from the initial stages of development to its completion.

Currently, electronic devices implement security in two distinct ways, namely from a software or hardware standpoint. To accomplish this objective, encryption algorithms have been integrated. It is possible to distinguish two distinct categories of encryption algorithms, namely symmetric and asymmetric algorithms.

In short, symmetric cryptographic techniques use a unique key for encrypting and decrypting messages. The most popular algorithms are the AES (Advanced Encryption Standard), DES (Data Encryption Standard), IDEA (International Data Encryption Algorithm), RC5 (Rivest Cipher 5), and TDES (Triple DES) not to cite them all. The key must be kept confidential and only shared among parties in order to maintain a confidential connection between them. The requirement for a single key is the main drawback of symmetric encryption methods. As a result, every possible step must be taken to safeguard key secrecy, such as avoiding key exchanges on public networks. However, symmetric encryption has a clear advantage over asymmetric encryption. As a result of utilizing a single key, symmetric algorithms are typically simpler than asymmetric algorithms, resulting in a reduction in computing power required for encryption. It is therefore possible to encrypt a large amount of data in a short amount of time.

In contrast, when it comes to symmetric cryptographic techniques, commonly referred to as public key cryptography techniques, a pair of keys is employed. The keys are usually referred to as public-key and private-key. The public key is used to encrypt a message, and anyone can use it. The private-key is, however, kept confidential

to ensure that only authorized parties can decrypt a message that has been encrypted with the public-key. The primary motivation behind having two keys is that it is impracticable to reconstruct the public-key from the private-key. The most commonly employed asymmetric algorithms include the RSA (Rivest–Shamir–Adleman) algorithm, the ElGamal encryption system, the ECC (Elliptic-curve cryptography), and the Cramer-Shoup system, to name a few. The main drawback of symmetrical algorithms is that they involve large mathematical calculations, which implies a higher time complexity. Hence, these techniques are capable of encrypting a limited quantity of data. Therefore, to achieve this objective, in the majority of systems, a hybrid approach is employed to employ both encryption methods, thereby ensuring optimal security and a brief calculation time.

On the one hand, if all the previously mentioned algorithms are mathematically reliable, their reliability will decrease when they are implemented on actual integrated circuits. Indeed, every integrated circuit uses electrical energy to function. Therefore, when an electric current appears in a conductor, there is inevitably an electromagnetic field associated with this current. Moreover, every measurable physical quantity concerning the IC could be a point of information leakage. This is particularly true when considering the fact that these quantities will exhibit varying variations based on the calculations performed by the IC. When evaluating these quantities, it is possible to retrieve confidential information. We described what is called a "**side-channel attack**" (**SCA**) when considering cybersecurity.

On the other hand, physical quantity measurement is not the only flaw in actual algorithm implementations. In fact, every physical IC has specifications under which it can execute its functions properly. It includes temperature, clock frequency, power supply voltage, and the electromagnetic environment. When pushed beyond its specifications, any integrated circuit will exhibit unpredictable behavior. However, it is still possible to control an IC's behavior outside its specifications with a certain degree of success. By doing so, it allows running the IC calculation incorrectly by finely controlling how much time and by which amount the IC is outside its specifications, thus enabling, with specific mathematical algorithms, to retrieve hidden data manipulated by the IC. This process is commonly referred to as a "**fault injection attack**".

We have identified two potential attacks on robust algorithms that have been implemented into actual integrated circuits. However, it is customary to categorize cyberattacks into three distinct categories based on their execution methods.

Despite being technically advanced, noninvasive attacks are the most materially trivial. SCAs are included in this set, which do not require any hardware modification to the targeted ICs, even if there is no physical contact. It is a delicate task to detect them; hence, they are deemed to be highly dangerous and are commonly considered in the initial stages of designing integrated circuits.

It is then possible to distinguish semi-invasive attacks. Systematically, they are accompanied by device physical preparation, which is entirely devoid of noninvasive attacks, but they are not accompanied by device physical modification. ICs integrity is therefore theoretically preserved. A typical IC modification involves the removal of the chip package. It enables access to either the front or back side of the integrated circuit, thereby facilitating micro-probing, laser injection, or substrate pulse injection. Furthermore, substrate thinning is also commonly considered and used, as it facilitates the fine-tuning of certain fault injection techniques, such as laser fault injection (LFI). These attacks necessitate specialized hardware, tools, and expertise and are frequently challenging to establish and execute.

Eventually, there are invasive attacks. They imply further physical modifications to integrated circuits. For instance, it is common to eliminate the layers of a chip, thereby enabling the photographing of the various layers and the reverse engineering of the target. A focused ion beam (FIB) can also be used to change the IC target internally by making electric connections that did not exist before. Contrary to semi-invasive attacks, invasive attacks frequently involve the definitive destruction of the target, primarily due to the absence of physical integrity during the process.

This doctoral thesis is dedicated to the study of a specific fault injection method: Body Biasing Injection (BBI). Within this context, we are going to study in this chapter the state-of-the-art concerning side-channel attacks as well as fault injection techniques described in the literature. This will allow us to explain the interests of the current work concerning hardware security.

In the first place, we will briefly present side-channel attacks. Then, we are going to take a closer look at various fault injection platforms commonly described. Eventually, we will ponder the interests of BBI in this context.

1.3 Side-channel attacks 2023-08-22 18:04:29+02:00

chap:1;sect:sca

1.3.1 Timing attacks 2023-08-22 18:04:29+02:00

chap:1;sect:sca;subsect:timingAttacks

The most fundamental side-channel attack has been first introduced in 1996 [3]. This attack consists in measuring the time duration required to perform cryptographic computations. By doing so, attackers were able to retrieve several algorithms keys, such as RSA. The calculation cost of this attack is light and allowed to perform fast attacks. Indeed, in RSA, as presented in [4], encrypting a message consists in calculating the following relationship:

$$C \equiv E(M) \equiv M^e \pmod{n} \quad \text{eqn:rsa(1.1)}$$

M being the message to be encrypted, C the ciphertext, and (e, n) the encryption key couple. The goal of the attack described in [3] is to retrieve e. To that end, the IC has to compute several times the equation 1.1 for different values of M, with identical values of e. The attacker has to measure each computation duration. If e is different for each operation, the attack cannot be performed. After the demonstration of this attack, countermeasures such as constant-time cryptographic algorithm, removing leak through timing analysis, and more recently, more advanced methods [5] have been proposed.

1.3.2 Power analysis and electromagnetic analysis attacks 2023-08-22 18:04:29+02:00

chap:1;sect:sca;subsect:powerAttack

Later, more elaborated side-channel attacks have been described in 1999 [6]. This paper introduces simple power analysis (SPA) and differential power analysis (DPA).

On the one hand, SPA consists in measuring and directly interpreting power consumption traces of a cryptographic IC. It allows, for example, counting DES or AES

rounds to get insights on the used implementation. In addition to this, it allows observing power consumption variation depending on executed instruction. Preventing simple power analysis has then been proposed, which consists in avoiding at all cost the use of secret keys or information when performing conditional branching logic.

On the other hand, DPA is a more elaborated method as it aims at identifying effects and variations related to data being processed by ICs. The aforementioned variations are more subtle and are often masked by noise. Therefore, DPA proposes to use statistics tools to reveal hidden system information, more specifically, it consists in computing the difference of means between traces. Preventing DPA is more complex than preventing SPA. One of the simplest methods is to add electrical noise. Another technique is to reduce measurable signal amplitude. It is done first by optimizing code execution, by finely choosing which operation is performed to reduce electromagnetic leakage. Second, it is also possible to shield the device, but it increases the IC's cost significantly.

In addition to these attacks, there is also another attack which is commonly studied: correlation power analysis (CPA) [7]. As well as DPA, CPA uses statistical tools. However, as opposite to computing the difference of means, it involves calculating the Pearson correlation coefficient (PCC), allowing to measure the linear correlation between different power consumption traces.

It is important to note that SPA, DPA and CPA are historically performed using traces directly measured from the ICs power consumption. However, these attacks can also be performed thanks to IC electromagnetic radiation analysis [8]. Because electric charges are circulating into the IC, they inevitably generate electromagnetic waves. Therefore, it is possible to pick up these waves, and similar to power consumption, their shape depends on the data being processed. There have been a lot of active researches concerning this method for twenty years. It can be explained thanks to its advantages compared to bare power consumption analysis. Indeed, when measuring the entire power consumption of an IC, it is not possible to target a specific area. It leads, especially with complex ICs and countermeasures, to an impossibility to perform such attacks. On the contrary, electromagnetic analysis attacks have multiple advantages over power consumption analysis attacks:

- No sample preparation required
- No physical contact with the target
- Require only little equipment: probe and voltage amplifier

As we stated previously, power consumption analysis attacks target an entire IC, whereas electromagnetic analysis attacks allow having fine resolutions. Indeed, the attack resolution is tied to the probe size, and it has been demonstrated [9]. In addition to that,

1.4 Fault-injection attacks 2023-08-22 18:04:29+02:00

chap:1; sect:fattack

Now that we have seen the basics of side-channel attacks, we are going to study fault injection techniques commonly described in the literature. Eventually, we are going to analyze how body biasing fault injection fits into this field.

II

Body Biasing Injection platforms and good practices 2023-08-22 18:04:29+02:00

chap:2_goodPractices

Contents

2.1	Summary <small>2023-08-22 18:04:19+02:00</small>	10
2.2	Introduction <small>2023-08-22 18:04:19+02:00</small>	10
2.2.1	Platform equipment <small>2023-08-22 18:04:19+02:00</small>	10
2.2.2	The hardware <small>2023-08-22 18:04:19+02:00</small>	10
2.2.3	The software <small>2023-08-22 18:04:19+02:00</small>	13
2.3	Body Biasing Injection enhanced practice <small>2023-08-22 18:04:19+02:00</small>	14
2.3.1	BBI practice in the state of the art <small>2023-08-22 18:04:19+02:00</small>	14
2.3.2	Enhanced BBI practice <small>2023-08-22 18:04:19+02:00</small>	17
2.3.3	BBI practices: a simple actual comparisons <small>2023-08-22 18:04:19+02:00</small>	18
2.4	Giraud's differential fault attack <small>2023-08-22 18:04:19+02:00</small>	20
2.5	Conclusion <small>2023-08-22 18:04:19+02:00</small>	22

2.1 Summary 2023-08-22 18:04:29+02:00

chap:2_goodPractices;sect:summary

This chapter first introduces multiple concepts, hardware and tools which are used and mentioned all along the work. Afterward, as its name implies, it brings forward better practices for Body Biasing Injection. It aims at introducing them with theoretical examples in addition to practical demonstrations. To that end, we propose to analyze different BBI platform scenarios thanks to coarse electrical models, allowing us to analyze their drawbacks and advantages in order to introduce the proposed enhancements. Eventually, we will present a real differential fault attack on a hardware AES co-processor in order to illustrate the soundness of the proposed improvements.

2.2 Introduction 2023-08-22 18:04:29+02:00

chap:2_goodPractices;sect:intro

2.2.1 Platform equipment 2023-08-22 18:04:29+02:00

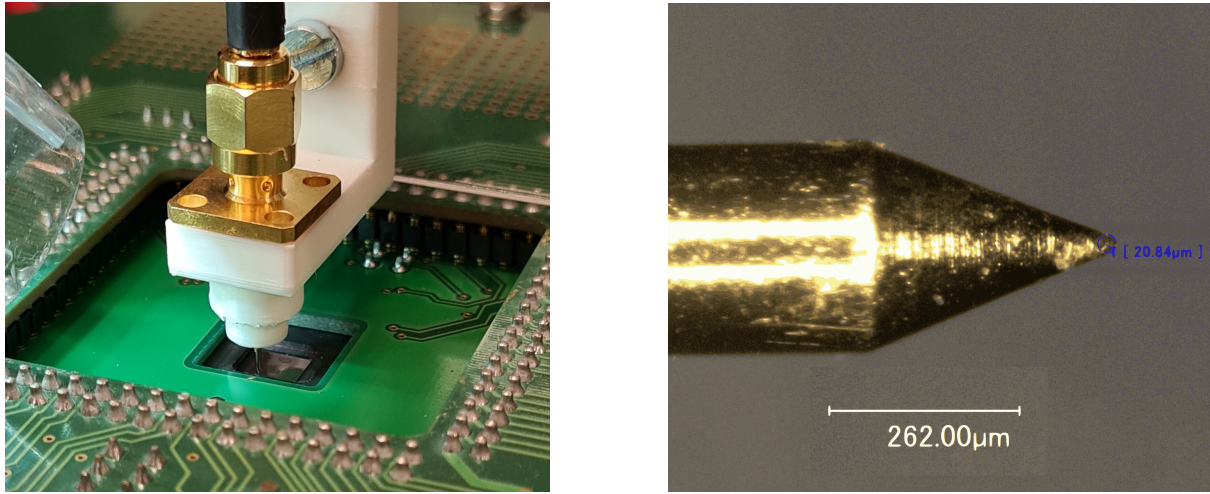
chap:2_goodPractices;sect:intro;subsect:platEquip

This section is dedicated to presenting the different pieces of equipment which allowed us to perform this work. The hardware platform, as well as the different software used, are introduced.

2.2.2 The hardware 2023-08-22 18:04:29+02:00

chap:2_goodPractices;sect:intro;subsect:platEquip,hardware

The main piece of equipment when working with BBI is the electrical probe. It is commonly made with a metal tip, a connector of any sort and a mechanical support to hold everything together. For this work, a custom probe was designed around three simple parts, an SMA connector, to have a low-cost, small and standard interconnection, a spring-loaded metallic probe soldered onto the SMA connector, and a custom 3D-printed support to hold the structure together. Fig. 2.1 shows detailed pictures of the designed BBI metallic probe, with a global view in operation on Fig.2.1a, and a photograph under a microscope of the probe's tip-end on Fig. 2.1b, allowing to measure its actual size before the first usage. The metallic probe used has a 0.635 mm diameter



(a) BBI metallic probe in mechanical contact with IC target
subfig:sondeBBI

(b) BBI metallic probe measurement closer look
subfig:pointeBBI

Figure 2.1: Dual-well and triple-well inverter silicon sectional view
Fig.sondePointeBBI

and is 16.35 mm long. The specified maximum nominal current of the probe is of 1.5 A, and the electrical contact resistance measures $70\text{ m}\Omega$.

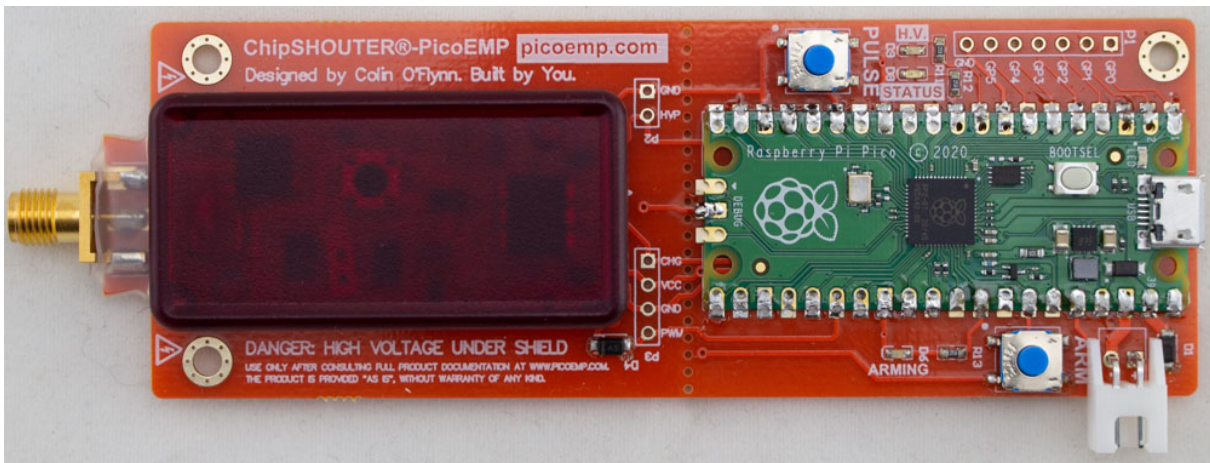


Figure 2.2: ChipSHOUTER®-PicoEMP from NewAE Technology Inc.
Fig.newAeChipShouter

Another fundamental piece of equipment for the practice of BBI is the voltage pulse generator. It is, generally, the most expensive hardware tool required. However, nowadays, cheap solutions are easily available, like the NewAE Technology Inc. ChipSHOUTER®-PicoEMP for example, illustrated in Fig. 2.2. In addition to being cheaper than most industrial solutions, its design sources are available online, making it a future-proof solution. In contrast to more expensive solutions, it has inevitably some drawbacks:

- The output transformer is low-power, around up to 200 mW

- Its recovery time is slow, from 1 to 4 seconds between pulses
- It can generate maximum voltage pulses of approximately 250 V
- There is no pre-calibration
- The pulse width control is not as reliable as other solutions



Figure 2.3: Front side of the Avtech Electrosystems Ltd. AVRK-4-B High Voltage Pulser Fig:avr4b

Nevertheless, for this work, the generator used in all experiments is from the company Avtech Electrosystems Ltd., specifically the model AVRK-4-B, shown in Fig. 2.3. It is a high-speed and high-voltage generator, specified to work with $50\ \Omega$ loads. Its main specifications are the following:

- Voltage pulse amplitude from 150 V to 750 V with positive and negative polarities
- Pulse width ranging from 6 ns to 20 ns
- Rise time (resp. fall-time) for positive (resp. negative) pulses of 4 ns
- Up to 1000 pulses per second
- GPIB remote control
- Propagation delay under 150 ns
- DC-coupled output

Then, the central piece of equipment of any fault injection method is the IC target. In our work, the focus was made on an STM32F439VIT6 LQFP100 microcontroller. It is a moderately modern IC commonly used nowadays. It was chosen because it embeds

a dedicated cryptographic core, able to do DES or AES, not to cite them all. The IC is manufactured with a bulk 90 nm process. Its core clock frequency goes up to 180 MHz, and it embeds 256 kB of RAM and 2 MB of Flash memory in two separate banks.

2.2.3 The software 2023-08-22 18:04:29+02:00

chap:2_goodPractices;sect:intro;subsect:platEquip,software

Because several simulations are performed for this work, different pieces of software are used. To perform every electrical simulations, we used Synopsys®'s PrimeSim HSPICE. It allows fast simulations with parallel calculation of large netlists. The computer used for these simulations is made around 48 cores, 96 threads CPU, alongside 420 GB of usable system memory. As we will study further in Chapter 3, the considered netlists are procedurally generated. To that end, we developed an algorithm, implemented in Python. It allows automatic generation of every netlist, minimizing user intervention, therefore drastically reducing errors, especially when considering the size of the simulated netlists. Indeed, they are not complex in their structure, as they are composed of resistors, capacitors and diodes, but the number of components ranges from one million for the smallest, to 4.7 millions for the biggest. The main limitation in simulating these netlists lies in the available system memory, as it is the first bottleneck to appear. In fact, simulating the smallest ICs takes up to 76 GB of memory during the transient simulation. As the memory usage scales linearly with the number of components, and because when doubling the width and height, the IC surface quadruples, the same applies for the components count. Therefore, simulating the biggest ones takes up to 420 GB of system memory, which represents an IC size of 1.1 mm by 1.2 mm. In addition to the memory consumption, the time required is also an important factor. Effectively, the smallest ICs take up to four hours and ten minutes with 8 CPU threads (which is close to the maximum HSPICE can do for our netlists). Then, because simulation time scales linearly with components count, the biggest IC takes up to 17 hours to be achieved.

2.3 Body Biasing Injection enhanced practice 2023-08-22 18:04:29+02:00

chap:2_goodPractices;sect:goodPractices

With the platform thoroughly introduced, we can now discuss the BBI practice in the state of the art compared to the enhancements we propose.

2.3.1 BBI practice in the state of the art 2023-08-22 18:04:29+02:00

chap:2_goodPractices;sect:goodPractices;subsect:stateoftheart

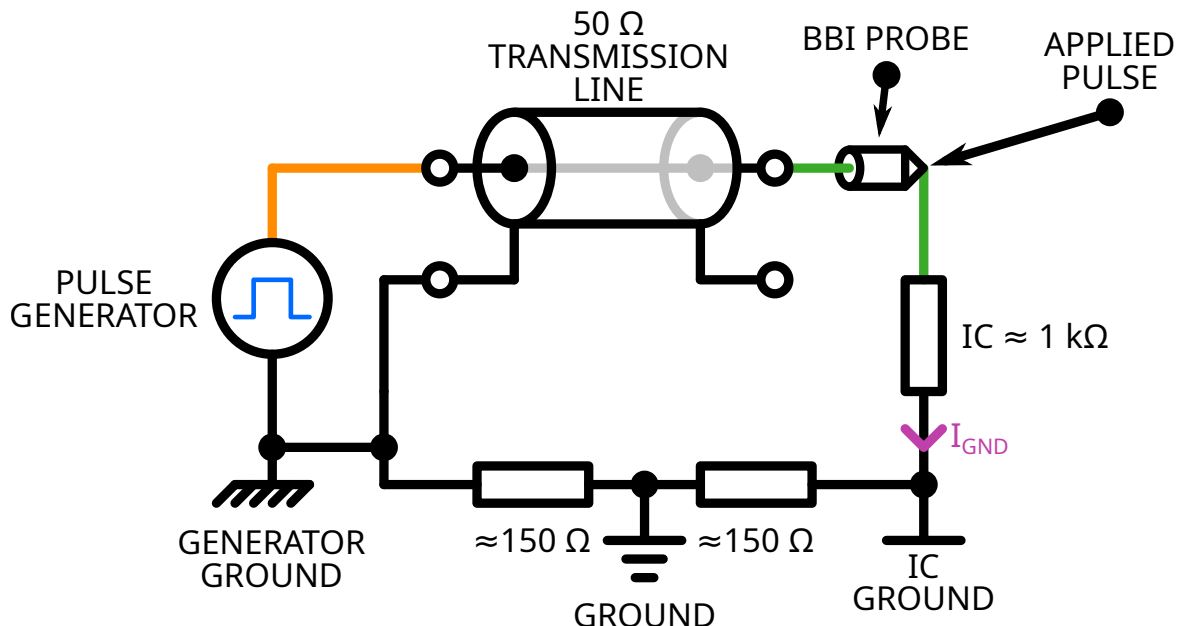


Figure 2.4: BBI platform example in the state of the art: schematic [fig:bbitracticeBadGnd](#)

First and foremost, in order to introduce the proposed enhancements, we will explain the limitations of state of the art BBI practices. Fig. 2.4 presents an example BBI platform as it is performed in the state of the art. This schematic only represents the main pieces of equipment, roughly composed of:

- A voltage pulse generator
- A transmission line
- A BBI probe
- An IC target
- A grounding setup

In that case, we want to bring forward two limitations of the platform as it stands. The first one is that most commercially available high voltage generator require a very specific load impedance to be used in order to meet their specifications, thus the 50Ω transmission line. However, the vast majority of integrated circuits substrates do not present at all times and in every location the exact required impedance for a specific generator.

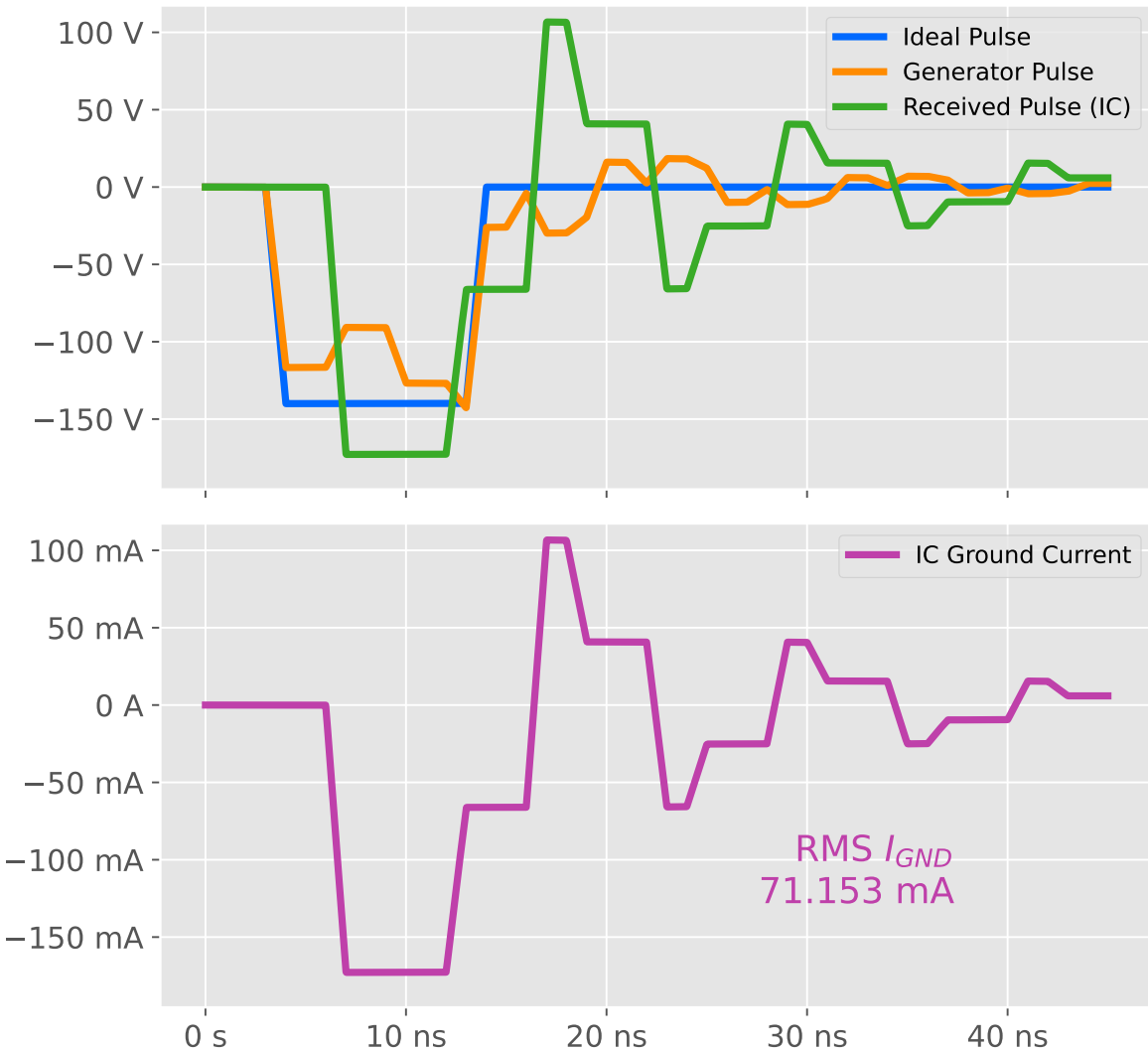


Figure 2.5: BBI platform example in the state of the art: simulation Fig.2.5.bbiPracticeBadGndSignals

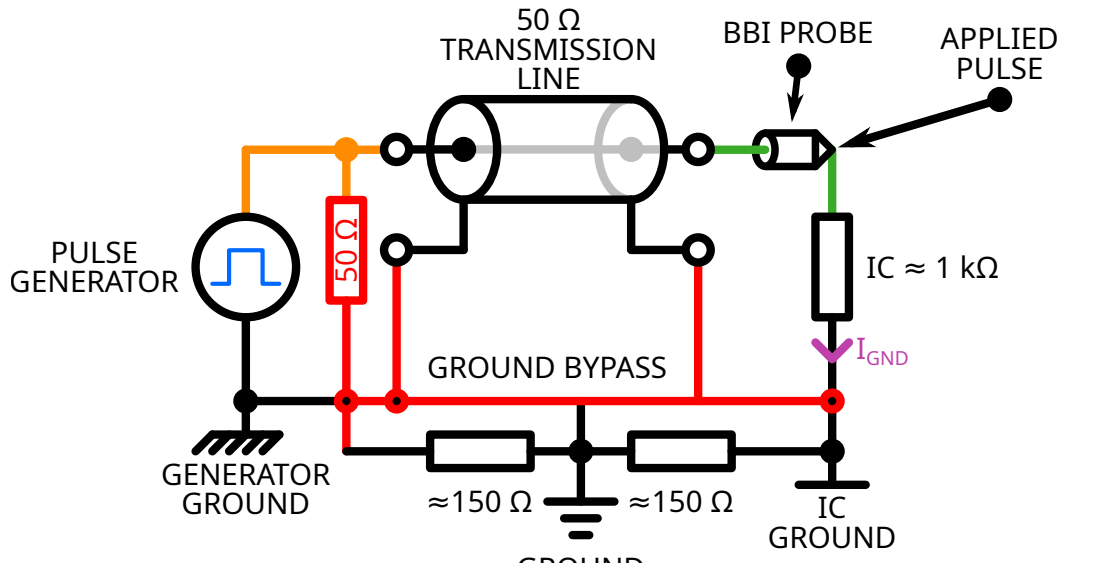
Therefore, impedance mismatch effects will inevitably show up, such as bounces in the transmission line. These effects are illustrated in Fig. 2.5. As one can notice, due to the bounces, there is a 25 % undershoot on the pulse received by the target (green signal), in addition to a 100 V overshoot. It is directly echoed on the IC ground current measurement (purple signal). However, one might wonder why this can be a

problem for the practice of BBI. The bounces in the transmission line, reflected in the IC current, are then propagated through the IC. Therefore, because the IC does not present in every substrate location a constant impedance, it is impossible to predict the bounces' shape. Thus, because an attacker has to achieve precise timing when injecting faults into an IC, and because of this impossibility to reach a certain degree of precision, it is highly problematic in a fault injection context. In order to mitigate this problem without increasing the platform's cost, we propose a very simple addition to the platform, consisting in connecting at the voltage pulse generator output a $50\ \Omega$ resistor in order to place the generator closer to its specifications.

The second limitation concerns the platform grounding. Contrary to impedance mismatching, it is a less predictable issue, as each platform will have very different grounding installation. Therefore, it is important to take measures to limit its side effects. In addition to worsening impedance mismatching, it can lead to a non-negligible limitation concerning energy transfer to the IC, by acting like a resistive voltage divider. Alleviating this limitation is simpler than matching the load impedance, as it only requires low-length, low-resistance ground interconnections to be made on top of the existing ones.

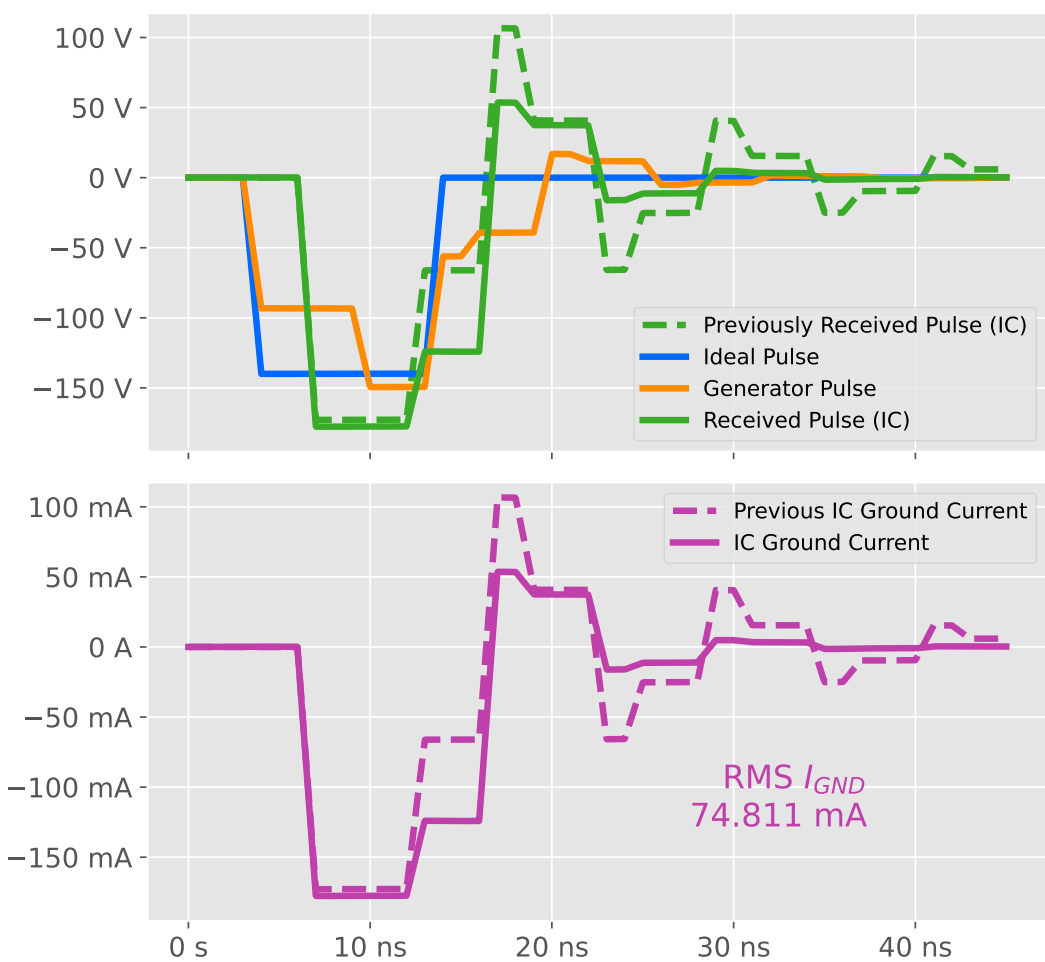
2.3.2 Enhanced BBI practice 2023-08-22 18:04:29+02:00

chap:2_goodPractices; sect:goodPractices; subsect:enhPractice



(a) Schematic

subfig:bbiBestPractice



(b) Simulation

subfig:bbiBestPracticeSignals

Figure 2.6: The proposed enhanced BBI platform

Fig:bbiBestPracticeDual

Fig. 2.6 illustrates the proposed improvements. The red nets on the schematic indicate the enhancements, and on the simulation results are shown in dotted lines the observed signals in the state of the art on top of the new signals in solid lines. What is important to remark here is first the significant bounces' reduction both on the IC received voltage pulse waveform and on the IC ground current waveform (which is an image of the received voltage due to the purely resistive nature of the simulated IC). Then, the effective injected current stays the same between both scenarios, which is expected. First because reducing the grounding impedance allows an increase in current, second because the approximate impedance matching reduces the injected current over time due to bounces' reduction.

2.3.3 BBI practices: a simple actual comparisons 2023-08-22 18:04:29+02:00

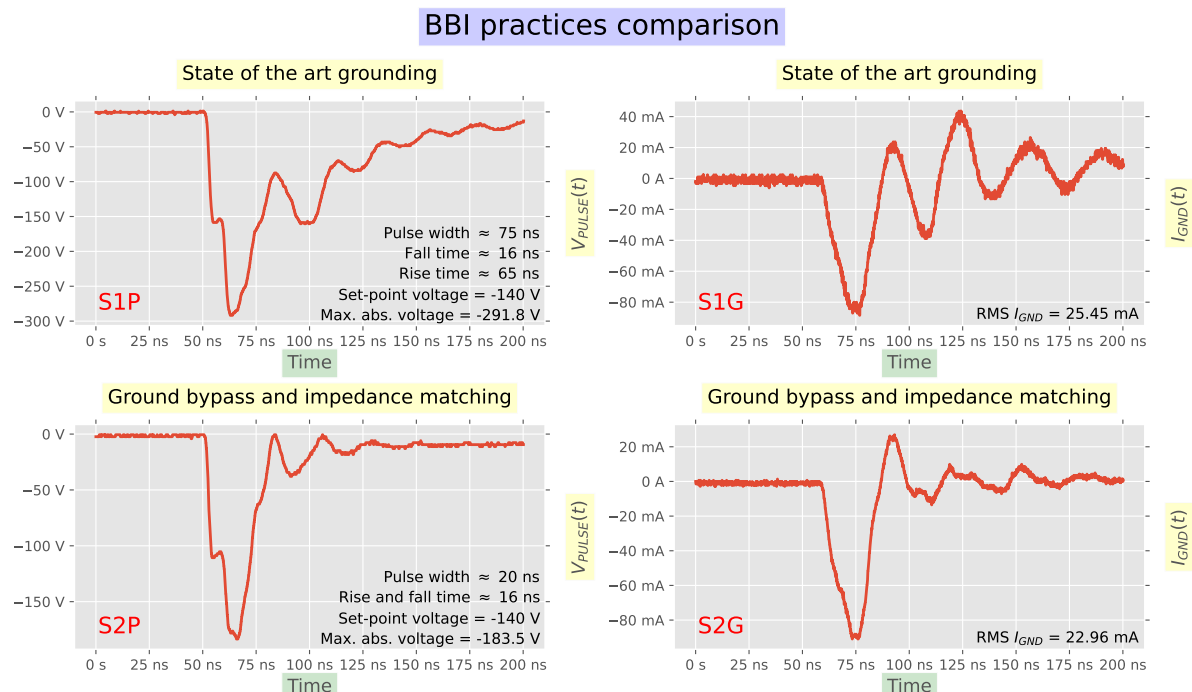


Figure 2.7: BBI enhancements with actual measurements fig:bbiRealXp

Evaluating the effects of the proposed enhancements through coarse platform simulations is the first step. However, in order to verify the models' soundness, we will analyze here practical experiments studying both cases. The equipment used is the one described in section ???. Fig. 2.7 displays the experimental results. Each signal is labeled in red starting with the letter S, followed by a number indicating the scenario (1

for the state-of-the-art and 2 for the enhanced practice), eventually followed by a letter indicating the signal type (P for the voltage pulse, G for the IC ground current). At the top of the Figure are shown the state-of-the-art signals, while at the bottom are shown the enhanced practice signals. The voltage pulse generator settings are the following:

- Required voltage set-point: -140 V
- Required pulse width: 20 ns
- Rise and fall times: 4 ns

The first interesting thing to notice here is that contrary to the voltage pulse generator, which is specified to deliver 4 ns rise and fall times, in both presented scenarios these measurements never reach the generator specifications.

Concerning the state-of-the-art practice, it is easily explained thanks to the bounces due to impedance mismatch between the generator and the IC, which can be observed on S1P and S1G. It results in a longer pulse than expected, whose width may vary depending on the injection location due to IC impedance variations. Therefore, the voltage pulse width is wider than requested. In addition to that, the maximum absolute voltage undershoots by 108 % compared to the requested set-point. Similar to the pulse width, voltage undershoot will greatly vary depending on the injection location. Eventually, when analyzing the current flowing out of the IC ground, it shows that the charges are going back and forth to between the IC and the generator, once again because of the bounces, which is an undesirable behavior when an attacker wants to create fast, short and precise disturbances into an IC.

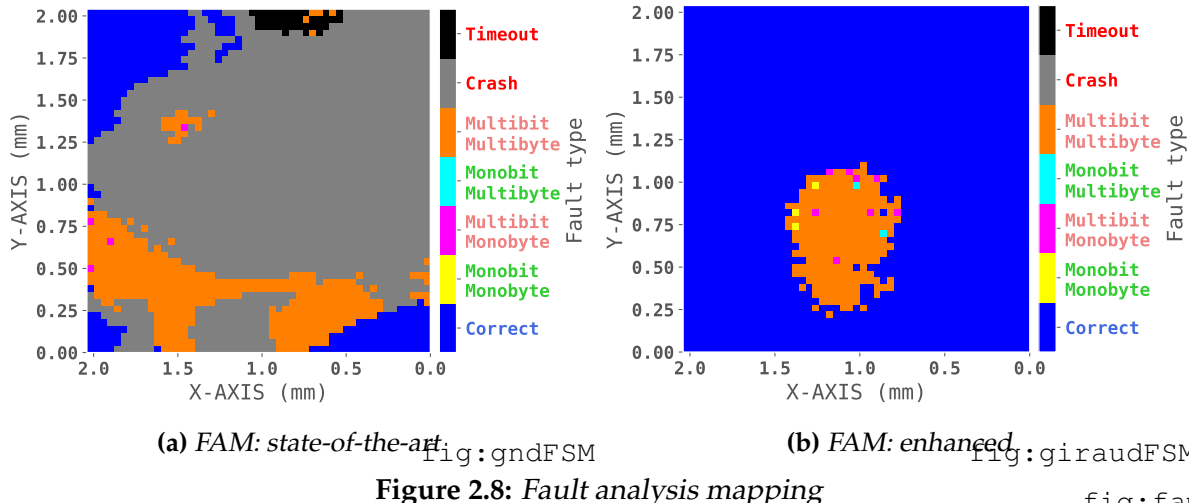
Concerning the proposed enhanced platform, the first remarkable information concerns the voltage pulse undershoot, which is reduced from 108 % to 31 %. It is mainly due to the approximate impedance matching, allowing the generator to work closer to its specifications. Then, even if the rise and fall times do not match the generator specifications, they are of equal length of 16 ns, which is more desirable than asymmetrical rise and fall times to produce precise pulses. The higher than expected value is mainly explained by the fact that the transmission line and the IC represent a far more complex impedance than a simple 50Ω termination resistor, especially when the IC impedance

presents a large capacitive component. The IC ground current is sharper with fewer bounces and fewer overshoots while the amount of charges transferred stays roughly the same (going from 25.5 mA_{RMS} to 23 mA_{RMS}).

2.4 Giraud's differential fault attack 2023-08-22 18:04:29+02:00

chap:2_goodPractices; sect:dfaGiraud

Now that we have seen the benefits of the proposed practice with a simple experiment, it is required, to further support these outcomes, to conduct in-depth experiments. To that end, we propose to compare the conduct and outcome of a differential fault attack, specifically the mono-bit Giraud's DFA as defined in the third section of [10].



To finely analyze how the IC behave to BBI, we performed experiments called Fault Analysis Mapping (FAM). Fig. 2.8 shows the FAM results for two scenarios: BBI in the state-of-the-art, and the proposed enhancements. For these experiments, the goal was to identify at each location the minimum set-point voltage required to induce a fault if possible, and the IC response to the disturbance. More specifically, these maps allow identifying in detail the AES response by detecting the nature of induced faults, if there are any. We can identify seven fault cases, described in Table 2.1.

Fault type	Description
Correct	The AES outputs a correct result
Mono-bit Mono-byte	The fault is located on a single bit on a single byte
Multi-bit Mono-byte	The faults are located multiple bits on a single byte
Mono-bit Multi-byte	The faults are located multiple bytes and are single bit
Multi-bit Multi-byte	The faults are located multiple bytes and multiple bits
Crash	The microcontroller did not respond correctly
Timeout	The microcontroller was unresponsive

Table 2.1: FAM faults description

table:faultType

Over the seven outcomes, only two can potentially lead to an exploitable fault according to Giraud's criterion: both single-bit scenarios. What is interesting to remark here is that these responses are either non-existent in Fig. 2.8a, or very rare in Fig. 2.8b. In addition to that, it is important to note that conducting such experiments take about 16 hours at best, up to 36 hours at worst. Therefore, to conduct the Giraud's attack, we decided, thanks to the second FAM including every proposed platform's enhancements, to linger on IC locations where Giraud's criterion was met and to dig further what could be achieved. This choice allowed us to perform the attack faster by only analyzing locations of interest.

For each valid location, a parameter sweep was performed, consisting in finding, for each set of parameters, as much single bit faults as possible. The following platform parameters were tested:

- The voltage pulse set-point: from -300 V to -600 V
- The pulse width: from 4.5 ns to 5.5 ns
- The injection time: $\pm 10 \text{ ns}$ before and after the penultimate AES round

For each set of parameters, we looked for at least one hundred single bit faults. However, in some cases, this goal was not achievable. To that end, we set a limit of ten thousand tests per set of parameters, allowing the algorithm to be finite.

As one can note, Fig. 2.8b shows five locations where valid faults were discovered. These points, only discovered thanks to an approximate experiment, do not represent the only interesting locations where the attack could be performed. If we put aside the FAM duration, performing the attack in itself is a fairly quick process. Indeed, in about 20 minutes, five sweeps were performed and 100 single-bit faults were obtained and analyzed for each interesting location. This allowed us to retrieve 14 bytes out of 16 bytes of the last round key. As stated in [10], for a 128 bits AES, finding the last round key means finding the key. The attack results are shown in Table 2.2.

	0	1	2	3	4	5	6	7	8	9	10	11	12	13	14	15
K10	0xFF	0x1F	XX	0xE8	0xEF	XX	0xA5	0x6A	0xCA	0xE7	0x55	0x3C	0xFD	0x65	0x39	0x26
KEY	0x01	0x23	0x45	0x67	0x89	0xAB	0xCD	0xEF	0xDE	0xAD	0xBE	0xEF	0x12	0x34	0x43	0x21

Table 2.2: Giraud's DFA results

table:dfaResults

The first row indicates the bytes numbers, the second the value of K^{10} bytes, and the last one contains the AES key in order to be able to compare the attack results to the encryption key.

Because only 14 bytes were found, we decided to perform other FAM to find other interesting locations. However, despite these additional experiments, we did not manage to find the two remaining bytes. Nevertheless, it is not interesting to try to find the two remaining bytes thanks to the Giraud's DFA. Indeed, we need to find 16 bits of the last round key, which are only 65536 combinations in the worst case. Considering our platform computer being able to perform $188 \cdot 10^3$ encryptions per second, it would take $\frac{2^{16}}{188 \cdot 10^3} \approx 349 \cdot 10^{-3}$ seconds to perform the required calculation in the worst scenario.

2.5 Conclusion 2023-08-22 18:04:29+02:00

chap:2_goodPractices; sect:conclusion

In this chapter, we first discussed the hardware and software commonly used for the practice of BBI, as well as presenting our hardware and software. We then proposed an enhanced platform for the practice of BBI, consisting of reducing the ground impedance and approximating the voltage pulse generator impedance matching. We

first studied these enhancements using a coarse platform. Furthermore, we then performed analog experiments using real hardware. In order to further verify the soundness of the BBI platform improvements, we set up and conducted a Giraud's differential fault attack. We observed that it would be impossible to conduct the attack without the aforementioned BBI platform enhancements, thus confirming their usefulness.

III

Integrated circuits modeling 2023-08-22 18:04:29+02:00

chap:3icModeling

Contents

3.1	Summary <small>2023-08-22 18:04:19+02:00</small>	26
3.2	Introduction <small>2023-08-22 18:04:19+02:00</small>	26
3.3	Electrical models <small>2023-08-22 18:04:19+02:00</small>	27
3.3.1	Standard-cell segment models <small>2023-08-22 18:04:19+02:00</small>	31
3.4	Preliminary model validation <small>2023-08-22 18:04:19+02:00</small>	35
3.5	Voltage pulse generator model and further validation <small>2023-08-22 18:04:19+02:00</small>	37
3.5.1	Early generator models <small>2023-08-22 18:04:19+02:00</small>	37
3.5.2	Further generator models and verification <small>2023-08-22 18:04:19+02:00</small>	38
3.6	Experimental comparisons <small>2023-08-22 18:04:19+02:00</small>	39
3.7	Conclusion <small>2023-08-22 18:04:19+02:00</small>	39

3.1 Summary 2023-08-22 18:04:29+02:00

This chapter presents the work carried out concerning the modeling and simulation of integrated circuits and platforms in a body biasing fault injection context. The presented work focused on elaborating electrical models allowing to evaluate with simulations the behaviors of ICs subjected to BBI. The chapter introduces the elaborated models and the algorithms used to create them, and then goes on to present various validation steps to check the meaningfulness of the models. Parts of this work have been published both in [1] and [11].

3.2 Introduction 2023-08-22 18:04:29+02:00

When evaluating and studying ICs under BBI, it is important to be able to fully predict and understand the underlying mechanisms at work in order to set up reproducible and reliable experiments, as well as being able to set up efficient countermeasures. However, to model and simulate integrated circuit behavior subject to fault injection is not an easy task. Specifically, simulating an entire IC at a transistor level under fault injection is unrealistic with current resources and technology. It is especially true when considering time cost, as current digital ICs are composed of about a million of transistors for standard microcontrollers. Furthermore, no software nor algorithm is currently dedicated to simulate the functional, electrical behavior of millions of transistors at the same time while some of them are disrupted by strong and transient disturbances. In addition to that, to be able to set up a reliable model, one should have access to the detailed architecture of each considered IC, which is almost never the case, as most studied architectures are proprietary. Therefore, it is required to find alternative workarounds in order to be able to study IC behavior and their various responses to fault injection techniques.

This has been first proposed in 2019 concerning Electromagnetic Fault Injection (EMFI) [12], and further extended in 2021 [13]. Especially in the latest work [13], the proposed solution consisted in establishing an equivalent non-logical model of the section of an IC. Instead of modeling each logic gate with as many transistors as required,

in addition to the power delivery network and the silicon substrate, it was chosen to represent a hundred of logic gates in an average way, solely with a few resistors and capacitors. This results in a transistor-less model, achieved using manufacturing data for the studied IC. The authors assumed that the first half of the transistors are conducting while the other half are blocking. Then, two levels of power delivery network were added, simply modeled with electrical resistances. Eventually, and because the modeled IC was manufactured using a dual-well substrate type, the silicon substrate and the P-N junction respectively are modeled by six resistors going in every direction in addition to a diode and its capacitance respectively. This clever design allows to drastically reduce the computing work required to analyze and predict behaviors of ICs subject to EMFI. Indeed, simulating the average behavior of a hundred of logic gates only with four resistors and four capacitors is immensely lighter than simulating the equivalent with BSIM (Berkeley Short-channel IGFET Model) transistors. However, the main shortcoming being the lack of functionality with the produced ICs, it is therefore impossible to evaluate their functional or logical behavior.

Body biasing injection being less documented than EMFI, no distributed model has yet been proposed to simulate ICs under BBI. In this context, our motivations were to set up and evaluate electrical models being able to reliably predict both in time and space IC behavior in order to understand how BBI induced disturbances propagate and create faults inside ICs. The current work main goal being to model and simulate BBI similarly to EMFI, we decided to start from the model proposed in [13], to improve and adapt it in order to be able to implement it in a BBI context.

This chapter begins with a general presentation of the enhanced models, followed by a closer look at each model and its specific features. Eventually, various model validation are studied in order to verify their soundness.

3.3 Electrical models 2023-08-22 18:04:29+02:00

sect : elecModels

On one hand, when performing EMFI (usually on the front side of the IC), air is the physical support to convey energy through electromagnetic waves. It is achieved

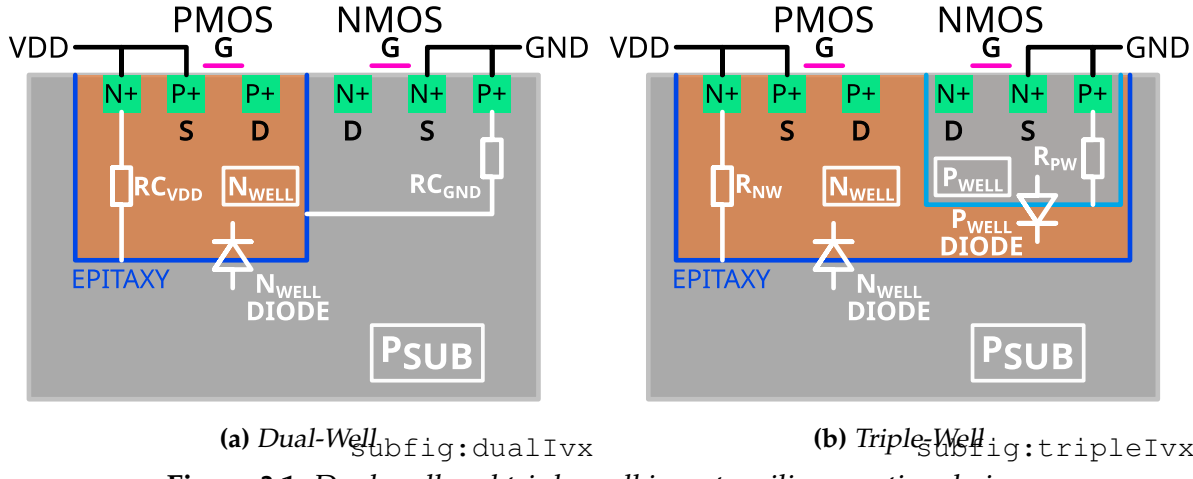


Figure 3.1: Dual-well and triple-well inverter silicon sectional view
Subfig: dualTripleIVx

by coupling the loop wire probe to the power delivery network loops. On the other hand, when working with BBI, the context is different. Indeed, the energy is conveyed through electrical charges through the silicon substrate. Therefore, the carriers have to go through the metallic probe and the whole substrate to reach the logic gates and the power delivery network in order to disturb the IC operation. Thus, the substrate type and design could have a significant impact on BBI efficiency. As a result, we explored and studied BBI in two specific scenarios depending on the substrate types: dual-well and triple-well. Fig. 3.1 shows the sectional views of two inverters manufactured in a dual-well and a triple-well substrate respectively. These simple schematics are helpful in understanding the reasoning behind the design of the electrical models.

Fig. 3.1a depicts the cross-sectional view of a dual-well CMOS inverter. The P-doped silicon substrate is colored in gray, with RC_{GND} being the access resistance from the epitaxy layer to the NMOS bulk. This physical environment is the conducting support of electrical charges which flow up to the NMOS transistor. The orange region is the N-doped silicon well, located inside the P-substrate to manufacture the PMOS transistors. RC_{VDD} is the access resistance from the epitaxy to the PMOS bulk inside the N_{WELL} . In addition to the P-substrate, the N-well is the last environment electrical charges have to go through before reaching the PMOS transistor.

Fig. 3.1b shows the cross-sectional view of a triple-well CMOS inverter. As before, gray areas represent P-doped silicon, and orange areas N-doped silicon. R_{NW} is the N_{WELL} access resistance from the epitaxy to the PMOS bulk, and R_{PW} is the P_{WELL} access resistance from the $N_{WELL} - P_{WELL}$ junction to the NMOS bulk. In this case,

two silicon junctions are present, represented by two independent diodes. In order to reach the PMOS transistors, charges have to go through the exact same environments as before. However, concerning NMOS transistors, they have to pass through two silicon junctions instead of none. As discussed in Chapter 5, this has a significant impact on BBI induced effects. However, these schematics are incomplete and do not allow simulating ICs behaviors under BBI.

Therefore, as it has been done in [13], ICs are spatially split in elementary sections called standard-cells segments (SCS). However, in addition to the improvement of the dual-well proposed model proposed in [13], we also introduce a triple-well model in order to fully appreciate the behavioral differences of BBI applied to both substrate types.

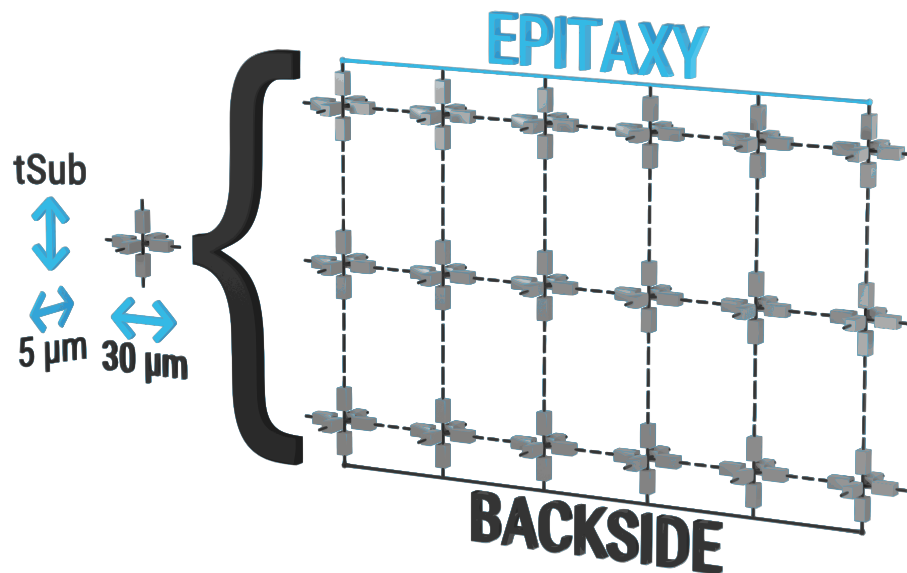


Figure 3.2: Surface subdivision improvement Fig: surfaceSubDivid

The main improvement over the dual-well model proposed in [13] concerns the substrate resistive network, as shown in Fig. 3.2. In [13], the substrate network is coarse and only consists of six electrical resistances for each SCS. It means that they represent the entire SCS substrate thickness, width, and height (on the left in Fig 3.2). Even though it is sufficient to appreciate the injection method effects while studying EMFI, mainly because the substrate is almost transparent when it comes to electromagnetic waves, but also because EMFI is mostly performed at the IC front side, it is not precise enough to model the spreading of the voltage pulse from the IC backside to the transistors.

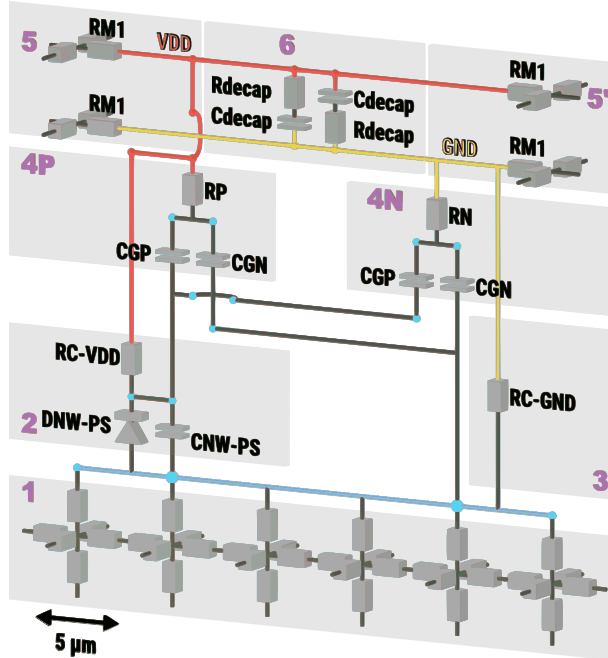
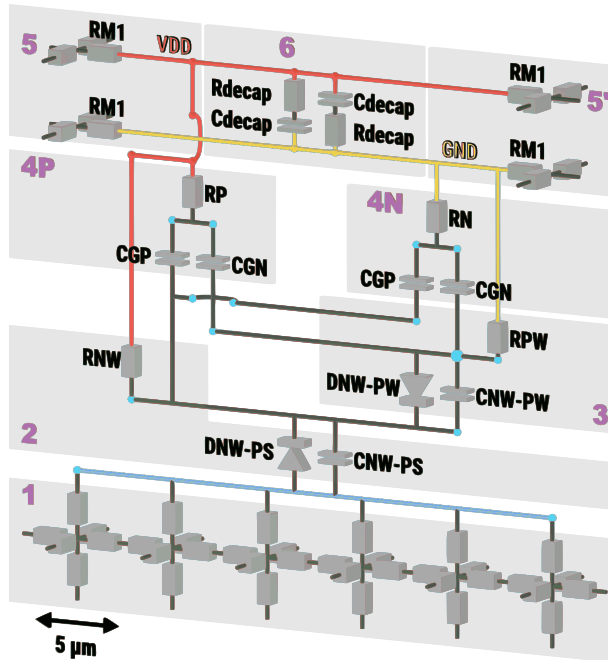
(a) Dual-Well_{Subfig:dualScs}(b) Triple-Well_{Subfig:tripleScs}

Figure 3.3: Three-dimensional Dual-Well and Triple-Well IC comprehensive standard-cell electrical schematic.
fig:dualTripleScs

To that end, we decided to split as much as possible these resistors, as shown in Fig. 3.2, to provide a precise enough substrate sub-model while keeping realistic computational workload. For the final models, it was decided to use an editable ele-

mentary thickness of $10 \mu\text{m}$, and fixed width and depth of $5 \mu\text{m}$ for each elementary six-resistors substrate models, according to the footprint of an SCS on the XY plane ($5 \mu\text{m} \times (6 \mu\text{m} \times 5 \mu\text{m})$), resulting in a $30 \mu\text{m}$ wide and $5 \mu\text{m}$ deep SCS. One can remark that in Fig 3.3, no number is given concerning the substrate thickness, as similar to LFI, it is an important parameter which does not have a fixed value. Indeed, an attacker may want to thin the substrate or not before performing BBI.

Furthermore, as shown in Fig. 3.3, both SCS models contain various electrical components describing the IC structure, roughly composed of:

- Its substrate
- Its silicon junction(s)
- Its logic gates
- Its power supply rails

These two models, while being close to each other, allow, thanks to their subtle differences, to properly consider the different behaviors each substrate type exhibits. In the next section, dual-well SCS model and triple-well SCS model are consecutively considered and analyzed.

3.3.1 Standard-cell segment models 2023-08-22 18:04:29+02:00

subSect: dualTripleWellScs

Historically, IC substrate was manufactured using an exclusive dual-well structure. However, nowadays, it is common to find on relatively modern ICs a mix of dual-well and triple-well structures on a monolithic die. Triple-well substrate structures bring significant advantages over dual-well substrates. In digital ICs, it is mainly used to body bias transistors to optimize their performance under power constraints. When used in analog or mixed designs, it gives two main advantages: substrate cross-talk and noise reduction, in addition to power supply decoupling thanks to the additional P-N junction capacitance [14]. This is why we decided to cover dual-well and triple-well structures in our models.

Fig. 3.3a depicts an SCS dual-well model. Each significant section of the SCS is gray-framed and numbered:

- The section [1] represents the substrate environment: resistive and isotropic.
- The section [2] is the $P - N$ silicon junction between the P-substrate and the N-well, represented by a diode and its junction capacitance, in addition to an access resistance $RC - VDD$, being the N-well electrical resistance.
- The section [3] is the substrate access resistance.
- The sections [4P] and [4N] contain the average non-logical model of a hundred of logic gates.
- The sections [5] and [5'] are the two levels of the power delivery network, which are low resistive metals.
- The section [6] is the decoupling between both GND and VDD power networks.

Fig. 3.3b depicts the SCS triple-well model as follows:

- The section [2] is the $P - N$ silicon junction between the P-substrate and the N-well, represented by a diode and its junction capacitance, in addition to an access resistance R_{NW} , being the N-well electrical resistance.
- The section [3] is the $N - P$ silicon junction between the N-well and the P-well, represented once again by a diode and its junction capacitance, in addition to an access resistance R_{PW} , being the P-well electrical resistance.
- The sections [1], [4P], [4N], [5'] and [6] being the same as before.

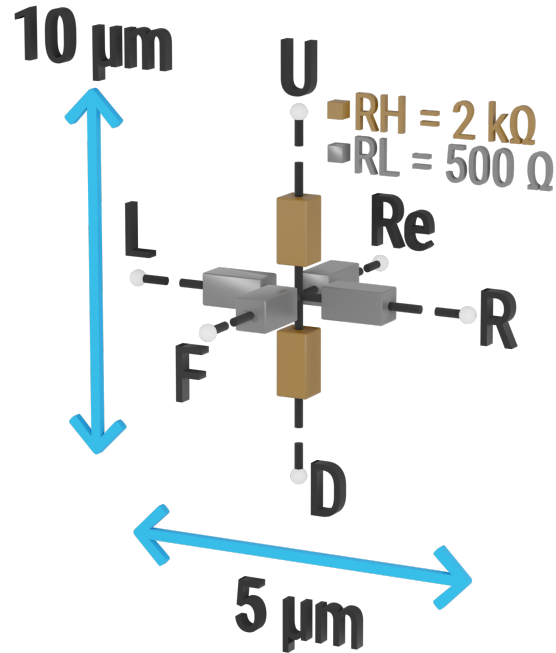
**Figure 3.4:** Elementary substrate 3D netlist

fig:algo

```
.subckt elementary_bloc D F L R Re U
R1 U N001 RH
R2 N001 D RH
R3 Re N001 RL
R4 N001 F RL
R5 N001 L RL
R6 R N001 RL
.ends elementary_bloc
```

Figure 3.5: Elementary substrate SPICE netlist

```
.subckt elementary_blocx6 D1 D2 D3 D4 D5 D6
+F1 F2 F3 F4 F5 F6 L R RE1 RE2 RE3 RE4 RE5 RE6
+U1 U2 U3 U4 U5 U6 VSUBCintC
XX1 D1 F1 L VSUBCintL2 RE1 U1 elementary_bloc
XX2 D2 F2 VSUBCintL2 VSUBCintL1 RE2 U2 elementary_bloc
XX3 D3 F3 VSUBCintL1 VSUBCintC RE3 U3 elementary_bloc
XX4 D4 F4 VSUBCintC VSUBCintR1 RE4 U4 elementary_bloc
XX5 D5 F5 VSUBCintR1 VSUBCintR2 RE5 U5 elementary_bloc
XX6 D6 F6 VSUBCintR2 R RE6 U6 elementary_bloc
.ends elementary_blocx6
```

Figure 3.6: SCS substrate layer SPICE netlist

fig:subSpiceSCS

Each area of the elementary SCS models were automatically generated using a custom algorithm, shown in Alg. 1. It was mainly designed in order to reduce as much as

possible any human intervention to limit difficult to debug errors and inconsistencies. Furthermore, it provides a degree of flexibility due to the ease of user modifications directly into the generation algorithm parameters, as opposed to netlist editing, thereby reducing errors further. These models only represent a section of an integrated circuit. For effective use and verification, it is necessary to replicate and interconnect these models spatially as much as possible. This was accomplished by utilizing customized Python scripts coupled with procedural generation. The IC generation algorithm enables the modification of multiple settings to produce the desired outcomes, albeit with certain inherent structural limitations. Two of the main limitations are the fixed width and depth of the elementary SCS models, and the fixed number of metal levels in the power delivery network. On the contrary, the following is a non-exhaustive list of user-modifiable settings:

- Global IC size.
- Probe position.
- IC global substrate thickness.
- IC elementary substrate thickness.
- Substrate type (dual-well, triple-well, or mixed).
- Voltage pulse amplitude.
- Voltage pulse width.
- Voltage pulse rise and fall times.
- Simulation time and step.

Eventually, the generator script incorporates a visual inspection tool in order to quickly verify the correctness of the generated netlist. Alg. 1 shows the IC generation algorithm main function, which is to create the coordinates for every net in the netlist.

3.4 Preliminary model validation 2023-08-22 18:04:29+02:00

Because validating such models is a complex task, we chose to trim validation into elementary steps. As these models aim at modeling and report back average IC behaviors, it is required to verify their soundness in trivial scenarios. Specifically, two class of measurements are going to be discussed in this section:

- Global quiescent leakage current evaluation
- Quiescent power network IR drop verification

These are important parameters to verify before going any further because any inconsistent or unrealistic value would result in meaningless models and simulations.

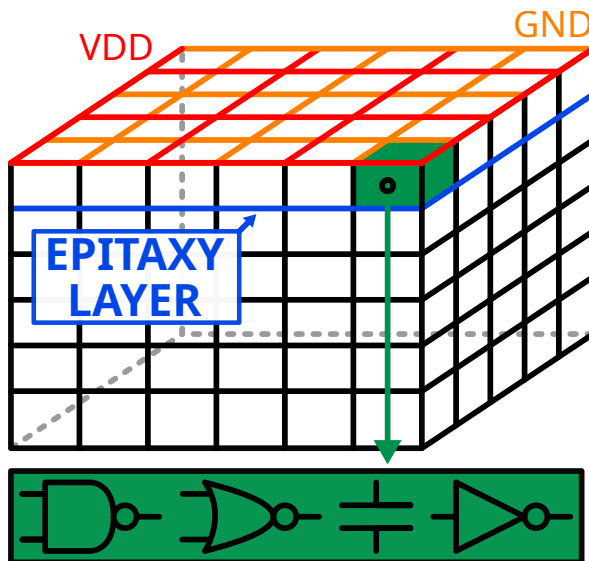


Figure 3.7: Three-dimensional standard-cell segments interconnection example. Fig. surfacesplitscs

To that end, we decided, as stated previously, to create an IC composed of several SCS. Fig. 3.7 depicts in a general way how the various SCS required are spatially connected to each other. In blue is indicated the epitaxy layer, which is the junction between the highest substrate level and the top of the SCS. All SCS share the power delivery network at their top and the silicon substrate at their bottom. As mentioned earlier, each SCS represent the average behavior of about a hundred of logic gates. The resulting IC measurements are the following: a width of $550 \mu m$, a depth of $450 \mu m$, and a thickness of $140 \mu m$. First, we will present the global leakage current, then,

we will analyze mappings of the simulated ICs power distribution networks. Dual-well, triple-well and mixed substrates models are analyzed, and most importantly, the simulated circuits do not include the voltage pulse generator nor any other external component required to work with BBI as what we present here is the first validation step. They are proposed as is, and Table 3.1 presents the operating point results for each substrate type.

Table 3.1: Dual-well, triple-well and mixed substrates SCS operating point.

Measurement	Description	Dual-well	Triple-well	Mixed substrates
I_{GND}	IC global ground current	1.92 nA	1.94 nA	3.4 nA
I_{VDD}	IC global VDD current	-1.96 nA	-5.8 nA	-3.5 nA
GND_{AVG}	Average GND voltage	1 nV	1 nV	1.75 nV
VDD_{AVG}	Average VDD Voltage	1.2 V	1.2 V	1.2 V

Looking at Table 3.1 indicates the absence of any significant leakage current and power supply voltage drop. However, to check the models relevance further and in a more reliable way, it is interesting to look at voltage mappings of the power delivery networks (VDD and GND), as shown in Fig. 3.8.

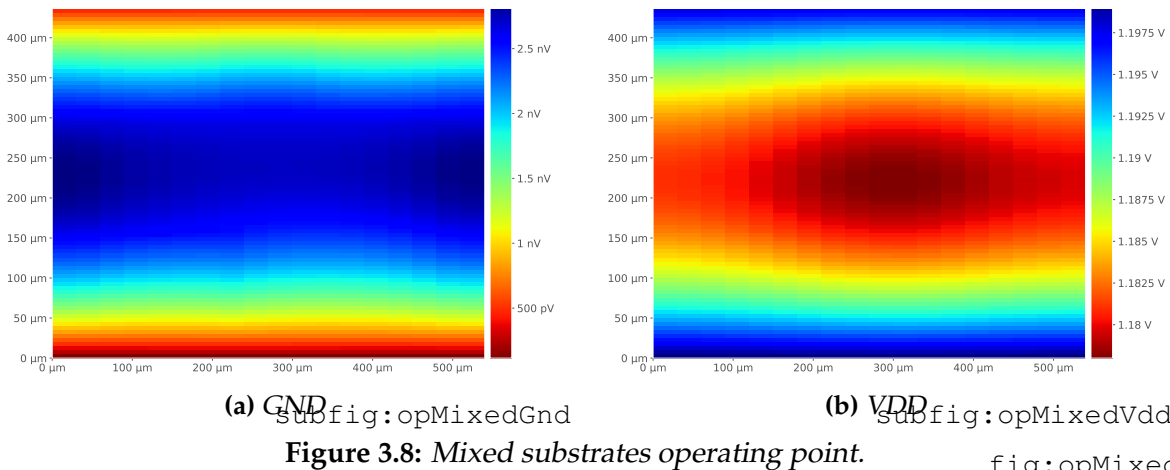


Figure 3.8: Mixed substrates operating point.

Concerning both GND and VDD operating point maps, there is no significant voltage drop across both maps, which indicates further the absence of significant leakage current in the simulated IC. With this in mind, we then introduced the generator into the model.

3.5 Voltage pulse generator model and further validation

2023-08-22 18:04:29+02:00

section:genModel

Introducing the generator did not come without major problems. Indeed, the latter inevitably interacts with the target IC, and depending on the real generator output stage architecture, this interaction can drastically vary from one to another.

For example, when using ESD guns as in [15, 16], their output stages are usually AC-coupled, while on our works, we mostly use DC-coupled generators. These subtle differences in practice become major issues in simulation when not treated correctly. Indeed, even considering the transmission line as it has been recommended in Chapter ??, most DC-coupled high voltage generators use a high-impedance mode to disconnect the load from the generator before and after the generated pulses. Therefore, one has to consider this specific aspect when designing a proper BBI electrical model, as we will explain in this section.

3.5.1 Early generator models 2023-08-22 18:04:29+02:00

subsection:earlyGenModel

The first models consisted in a PWL voltage source directly connected to the substrate of the IC, and we quickly observed abnormal operating point values. **Je dois rajouter des valeurs chiffrées.** Indeed, in this setup, at rest, the generator is equivalent a DC voltage source applying 0 V to the backside of the simulated IC. Therefore, it applies an undesired bias to the substrate and thus changes the operating point, inducing a high amount of charges flowing between power sources, thus disturbing the power delivery network. To circumvent this issue, we chose to mimic the behavior of an actual high voltage pulse generator and to switch between a high impedance mode and a voltage pulse mode as a function of the pulse time. This allowed to observe correct operating points with the generator connected, as it is the case in a real experiment. **Je rajouterais les figures.**

3.5.2 Further generator models and verification 2023-08-22 18:04:29+02:00

subsection: furtherGenModel

Because the previously explained generator model is electrically perfect and does not include any impedance mismatching effects, we extended the model to include the generator output impedance and the transmission line. *Peut-être faire un schéma ?* It allowed us to observe impedance mismatch effects, which are of great importance when performing BBI (Chapter ??), as the injected pulses are very fast and of high amplitude. Thus, impedance mismatch greatly changes the effective applied voltage pulse and injected currents, while also modifying unpredictably the induced disturbances, as we will observe further in this manuscript.

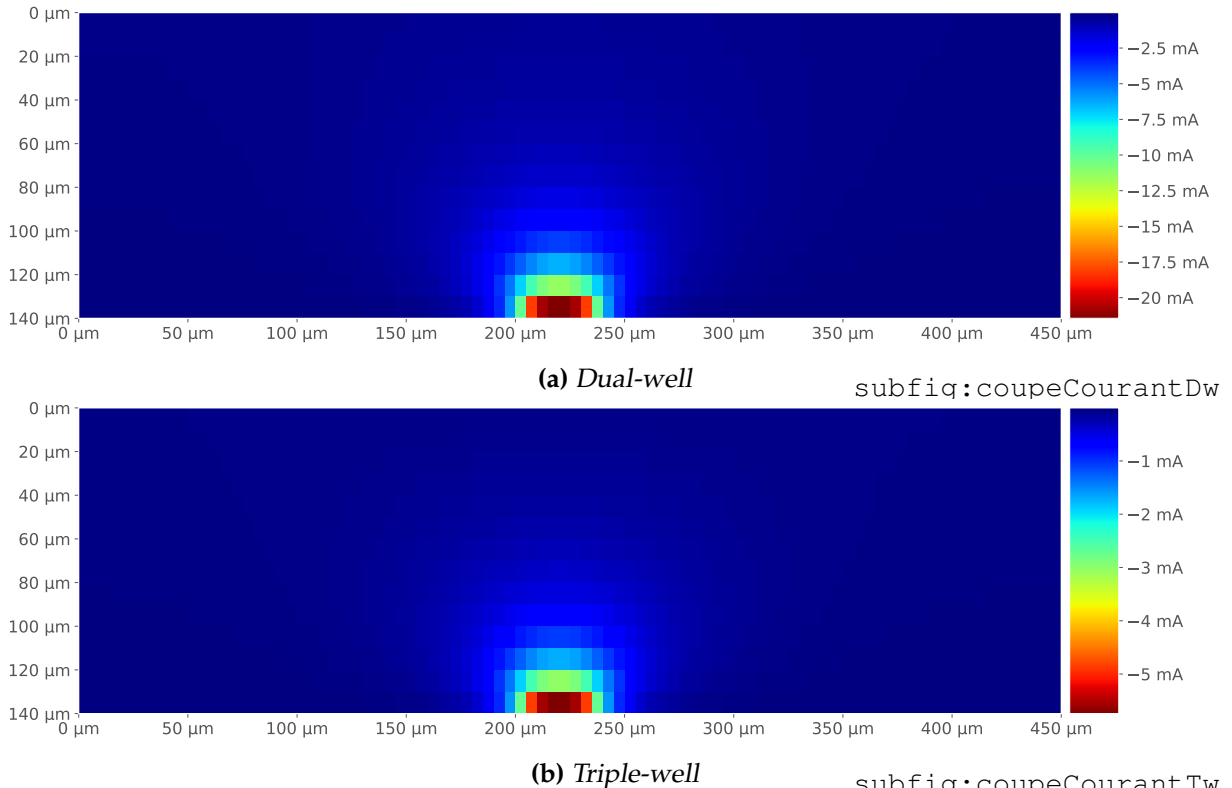


Figure 3.9: Dual-well and triple-well cross-sectional current distribution view at the apex of the voltage pulse

fig:coupeCourantDwTw

In order to verify more thoroughly the soundness of the proposed models, a circuit under BBI is simulated in order to analyze the current distribution and amplitude, specifically at the peak of the voltage pulse. Fig. 3.9 presents the results for both dual-well and triple-well ICs. The substrate being a resistive environment, it is natural to observe isotropic hemispheric current distributions. However, it is interesting to notice that the results show a lower amount of current concerning the triple-well IC

compared to the dual-well one. It can be explained thanks to the coupling between the probe/substrate and the logic gates. On one hand, as shown in Fig. 3.1, in the dual-well IC, the charges do not have to cross any silicon junction in order to reach the NMOS transistors, while there is one junction between the probe and the PMOS transistors. On the other hand, concerning the triple-well IC, there is always at least one silicon junction to cross in order to reach the transistors. Because of this, and because the voltage pulse will inevitably bias the diode, it will change the coupling whether the diode is conducting or blocking. When the diode is conducting, the transistors are DC-coupled to the probe, whereas when the diode is blocking, the transistors are AC-coupled. In the second case, it means that charges can flow only on the edge of the pulse. Thus, during the pulse's plateau, there is no charge flow.

3.6 Experimental comparisons 2023-08-22 18:04:29+02:00

CREUSER PLUS EN DÉTAILS DANS LES SECTIONS PRÉCÉDENTES LES DIFFÉRENCES DUAL/TRIPLE, PARCE QUE C'EST IMPORTANT DANS LE MODÈLE ! In order to complete this chapter, we are going to analyze, in this last section, experimental results highlighting the differences between dual-well and triple-well substrates.

3.7 Conclusion 2023-08-22 18:04:29+02:00

In this chapter, we presented enhanced electrical models which can be utilized to simulate integrated circuits under body biasing fault injection. These models, supported by older ones originally designed for ICs under EMFI, cover two substrate types commonly found in commercial ICs: dual-well and triple-well substrates. The substrate type is of great importance when considering BBI as it is the only physical environment where charges can circulate. Each sub-models contain:

- The power delivery network
- The average electrical model of a hundred of logic gates

- The various silicon junctions
- The silicon substrate

Standard-cells segments models representing a portion of an IC, they need to be replicated and connected with each other in order to be meaningful. In addition to this, they propose refined substrate sub-models in order to improve the model spatial accuracy over their predecessors. The main advantage of these models is their relative lightness, computationally speaking. Indeed, they are only composed of passives components, in order to be able to simulate large resulting ICs. However, their main advantage is also their main shortcoming, they do not represent any function of the modeled IC, but its average electrical behavior.

Algorithm 1 Integrated circuit SPICE netlist generation algorithm.

alg:icGen

Require: SUBTYPE
Require: TSUB
Require: ESUB
Require: VPUU
Require: PW
Require: TFR
Require: SIMTIME
Require: SIMSTEP
Require: TEX
Require: TEY
Require: prbX
Require: prbY

$RH \leftarrow 2000$ ▷ Elementary substrate up-down/front-rear resistor value
 $RL \leftarrow 500$ ▷ Elementary substrate left-right resistor value
 $WSEG \leftarrow 30$
 $HSEG \leftarrow 5$
 $W6SEG \leftarrow 30 \div 6$
 $nC \leftarrow TEX \div WSEG$ ▷ Number of column
 $nL \leftarrow TEY \div HSEG$ ▷ Number of lines
 $nH \leftarrow TSUB \div ESUB$ ▷ Number of substrate layers

Ensure: nC, nL and nH are integers

```

var SCS[nL, nH]      ▷ Array containing each standard-cell properties
RH  $\leftarrow RH \times (ESUB \div 10)$       ▷ Adjust RH value according to user defined variable
RL  $\leftarrow RL \times (ESUB \div 10)$       ▷ Adjust RL value according to user defined variable
for all cY in  $[0 ; nL]$  do
    for all cX in  $[0 ; nH]$  do
         $\vec{X} \leftarrow \begin{bmatrix} cX \times WSEG \\ cX \times WSEG + 1 \times (W6SEG \div 2) \\ cX \times WSEG + 3 \times (W6SEG \div 2) \\ cX \times WSEG + 5 \times (W6SEG \div 2) \\ cX \times WSEG + 7 \times (W6SEG \div 2) \\ cX \times WSEG + 9 \times (W6SEG \div 2) \\ cX \times WSEG + 11 \times (W6SEG \div 2) \\ cX \times WSEG + 12 \times (W6SEG \div 2) \end{bmatrix}$ ;  $\vec{Y} \leftarrow \begin{bmatrix} cY \times HSEG \\ (cY + \frac{1}{2}) \times HSEG \\ (cY + 1) \times HSEG \end{bmatrix}$ 
        if  $\vec{Y}[0] = 0 \vee \vec{Y}[0] = TEY$  then      ▷ Determines if SCS has external power
            SCS[cY, cX].power = True
        else
            SCS[cY, cX].power = False
        end if
        if  $\vec{X}[0] = prbX \wedge \vec{X}[2] = prbX \wedge \vec{Y}[0] \leqslant (prbY + 15) \wedge \vec{Y}[0] \geqslant (prbY - 15)$  then
            SCS[cY, cX].probe = True
        else
            SCS[cY, cX].probe = False
        end if
    end for
end for
```


IV

Substrate thinning analysis 2023-08-22 18:04:29+02:00

chap:4thinning

Contents

4.1	Summary <small>2023-08-22 18:04:19+02:00</small>	44
4.2	Introduction <small>2023-08-22 18:04:19+02:00</small>	44
4.3	Geometric and electrical modeling <small>2023-08-22 18:04:19+02:00</small>	45
4.3.1	Geometric modeling <small>2023-08-22 18:04:19+02:00</small>	45
4.3.2	Electrical approach <small>2023-08-22 18:04:19+02:00</small>	49
4.4	Models validation <small>2023-08-22 18:04:19+02:00</small>	51
4.4.1	IC substrate thinning quick look <small>2023-08-22 18:04:19+02:00</small>	51
4.4.2	Experiments with thinned circuits <small>2023-08-22 18:04:19+02:00</small>	52
4.5	Conclusion <small>2023-08-22 18:04:19+02:00</small>	54

4.1 Summary 2023-08-22 18:04:29+02:00

This chapter proposes to study the interests of thinning the substrate of integrated circuits with the aim to enhance Body Biasing Injection efficiency. First, we are going to present a geometrical approach in order to appreciate with a certain abstraction from electronics the effects of substrate thinning on ICs behaviors. Second, thanks to the models presented in Chapter 3, in addition to the geometrical approach, we are going to theoretically analyze the effects of substrate thinning from an electrical point of view. Eventually, in order to verify the soundness of the geometric approach and the simulation results, experiments are going to be studied thanks to an actual analysis of substrate thinning on identical IC targets behavior.

4.2 Introduction 2023-08-22 18:04:29+02:00

When working with integrated circuits in a fault injection context, several physical parameters of the considered IC are of great importance. For example, as we have seen in the previous Chapter, the type of substrate used to manufacture the IC has a significant impact on BBI efficiency and behavior. In addition to this, the transistors' size, power supply voltage, the IC package or the IC substrate thickness can drastically change fault injections results. Among these examples, one of great interest for body biasing injection is the substrate thickness.

Indeed, as there are different manufacturing processes depending on the purpose of each manufactured IC, it is common to find various substrate thicknesses depending on the IC targeted application. On one hand, it is not rare to find 700 µm thick wafers with 300 mm diameters for generic applications. On the other hand, in other specific applications like SoCs, where vertical stacking is commonly used, or in Smart-cards and ID cards, the typical substrate thickness value is lower, around 200 µm. In addition to these differences one can find in commercial products, the practice of thinning the substrate of ICs is not uncommon in a context of fault injection. More specifically, substrate thinning has been thoroughly studied concerning Laser Fault Injection (LFI) [17, 18], and has proven to greatly enhance LFI efficiency, in addition to drastically

reducing the power required to create faults. However, it had not been studied for Body Biasing Injection at the beginning of this work.

In this context, this work was first done in order to assess whether substrate thinning has similar effects on BBI as it has on LFI. Second, because thin ICs commonly found in smart-cards have unavoidable security constraints, third because BBI is performed using the silicon substrate as the physical environment to carry energy through electrical charges. Therefore, this Chapter will evaluate the interests of substrate thinning on BBI efficiency. In other words, we will analyze the electrical and behavioral differences between identical ICs with different substrate thicknesses. This analysis will take place using multiple approaches. In the first place, we will address the question using a geometric approach to appreciate the effects of substrate thinning on voltage propagation inside the substrate while taking a step back from electrical modeling. Then, the geometric approach will be completed with an electrical simulation analysis of two identical ICs with different substrate thicknesses, created thanks to the models proposed in Chapter 3. Eventually, experimental results will be analyzed in order to verify the correctness of the previous approaches, in addition to studying the actual effects of substrate thinning concerning faults creation.

4.3 Geometric and electrical modeling 2023-08-22 18:04:29+02:00

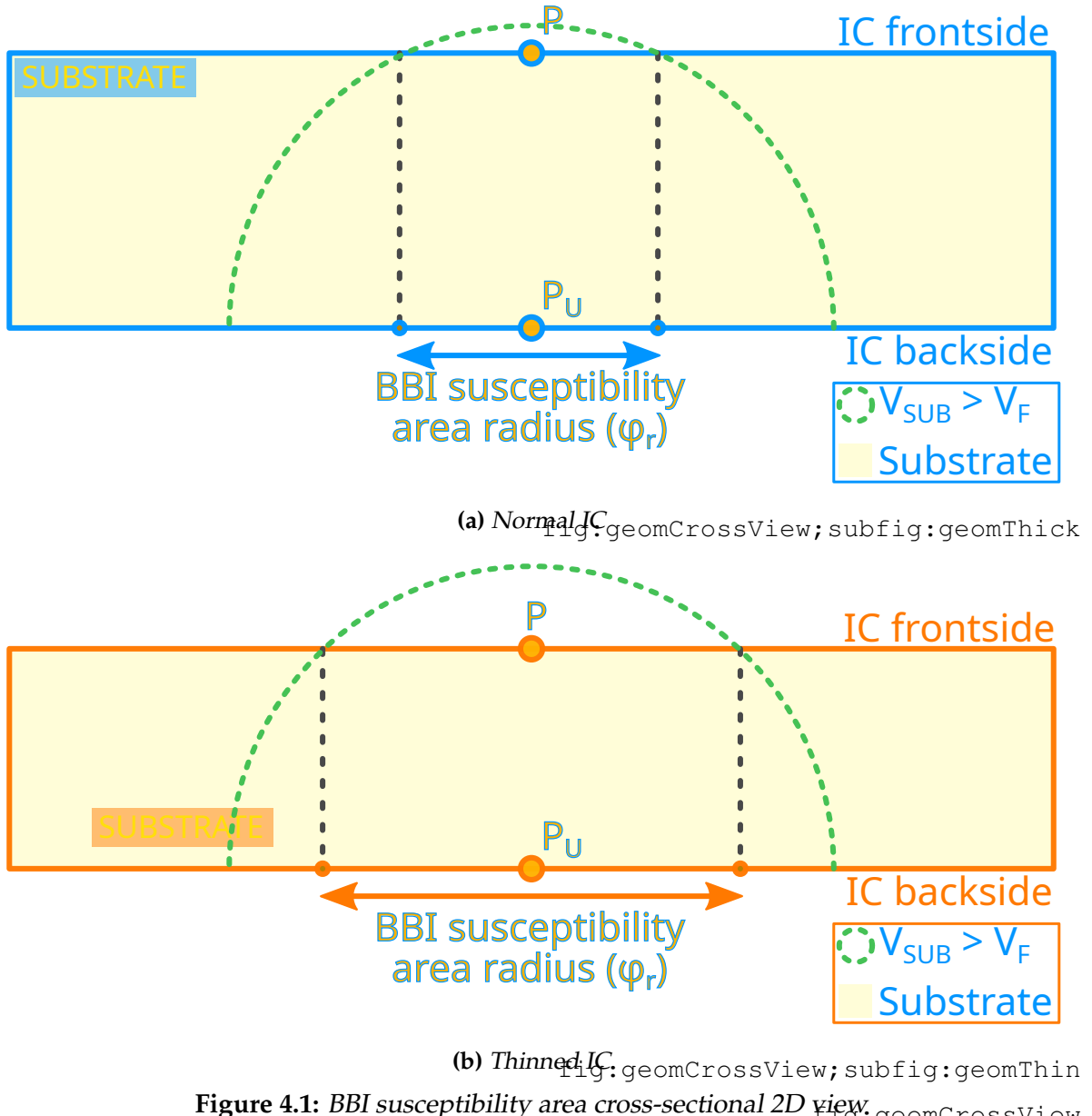
chap4 : sect : geomModel

To begin with, we will address the geometric approach. It has been chosen thanks to the advantages it brings forward, such as the abstraction from electronics it enables, thus allowing easier and faster modeling. However, because this approach alone is insufficient, we will then study an analogous electrical one.

4.3.1 Geometric modeling 2023-08-22 18:04:29+02:00

chap4 : sect : geomModel : subsect : geomModel

For the purpose of geometric modeling, let us consider two identical ICs. A commercial one, with an arbitrary standard substrate thickness, and another one with its substrate thinned by a certain amount in order to perform fault injection. Fig. 4.1 illustrates



the two-dimensional cross-sectional views of the considered ICs substrates during an arbitrary BBI voltage pulse. The silicon substrate being an isotropic resistive environment, it is quite natural to expect the electrical charges to flow and spread evenly when injected into it at any given time. Therefore, equipotentials form half-sphere surfaces inside the substrate volume. These surfaces are highlighted in two-dimensions as green half-circles in Fig. 4.1.

In this scenario, an attacker wants to induce a fault in the logic gates, located at the top of each IC. To that end, they need to change the voltage enough at point P , called V_P , in order to disturb the transistors and change the logic gates behavior. In addition

to that, and for the sake of simplicity, let us assume that P is the only location in the considered IC where faults can be injected. However, in order to observe faults at point P , V_P needs to reach a minimal threshold voltage, called V_F . Because the attacker is working with BBI, a metallic probe is connected onto the backside of the IC, at point P_U , in order to inject energy into the IC. Depending on the amount of injected energy, in other words, the maximum amplitude of the voltage pulse because the substrate effective resistance is static, the voltage at P might never reach V_F , therefore, no faults will be observed. Let us consider that the attacker chose an amplitude V_{PU} big enough such that at a moment in the injection, V_P reaches V_F or more in each considered IC. In that scenario, the area on the IC front side where $V > V_F$ is a disk of radius ϕ , centered in P , called the BBI susceptibility area radius. It means that the attacker can position the probe anywhere on the backside within this disk to reach V_F at P , and therefore induce a fault at P .

The half-sphere equipotential radius relative to time can be determined thanks to the following formula:

$$r(t) = \frac{\rho_{SUB}}{\sqrt{2}} \cdot \frac{|I_G(t)|}{|V_{PU}(t) + V_F|} \quad (4.1)$$

with ρ_{SUB} the resistivity of the silicon substrate, $I_G(t)$ the instantaneous sum of the current distribution contained in the half-sphere, and $V_{PU}(t)$ the instantaneous voltage pulse applied on the backside of the IC. Then, logically, the BBI susceptibility area radius, denoted ϕ_r , is described by:

$$\phi_r(t) = 2 \cdot \sqrt{r(t)^2 - t_{SUB}^2} \quad (4.2)$$

with t_{SUB} being the IC substrate thickness.

As it is illustrated in Fig. 4.1, thinning the substrate inevitably increases the size of the susceptibility area if the experimental conditions are constant. It means that the susceptibility evolution ratio is always greater than 1 when thinning the substrate:

$$\frac{\phi_r^{THIN}}{\phi_r^{THICK}} = \sqrt{\frac{r^2 - t_{THIN}^2}{r^2 - t_{THICK}^2}} > 1 \quad (4.3)$$

Therefore, in order to obtain the same susceptibility area with a thinner IC, it is

required to reduce the voltage pulse amplitude, thanks to the following relation:

$$V_{PU}^* = \frac{t_{THIN}}{t_{THICK}} \cdot V_{PU} + V_F \cdot \left(1 - \frac{t_{THIN}}{t_{THICK}}\right) \quad (4.4)$$

Eventually, this geometrical approach allows deducing three conclusions:

1. Thinning the substrate allows reducing the minimal voltage pulse amplitude required to induce a fault while keeping a constant susceptibility area.
2. The BBI susceptibility area increases while the substrate thickness decreases while working at a constant voltage pulse V_{PU} .
3. Thinning the substrate alone does not have an influence on BBI spatial resolution, as the susceptibility area depends on the couple (t_{SUB}, V_{PU}) . Thus, similar spatial resolution could be obtained with different substrate thicknesses by changing V_{PU} .

4.3.2 Electrical approach 2023-08-22 18:04:29+02:00

chap4:sect:geomModel:subsect:elecApproach

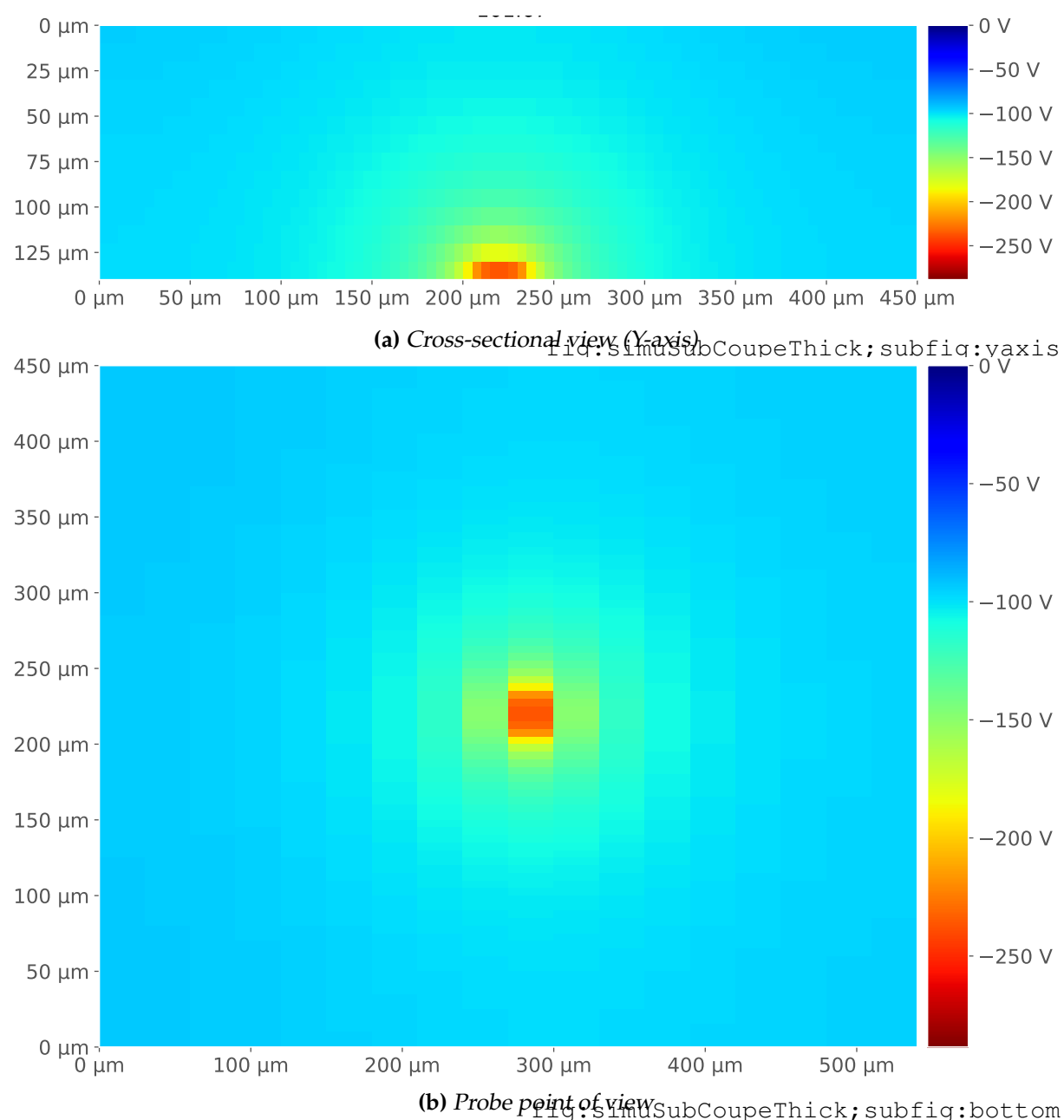


Figure 4.2: Simulated non-thinned IC (140 μm) substrate voltage distribution: peak of the first voltage pulse edge

fig:simuSubCoupeThick

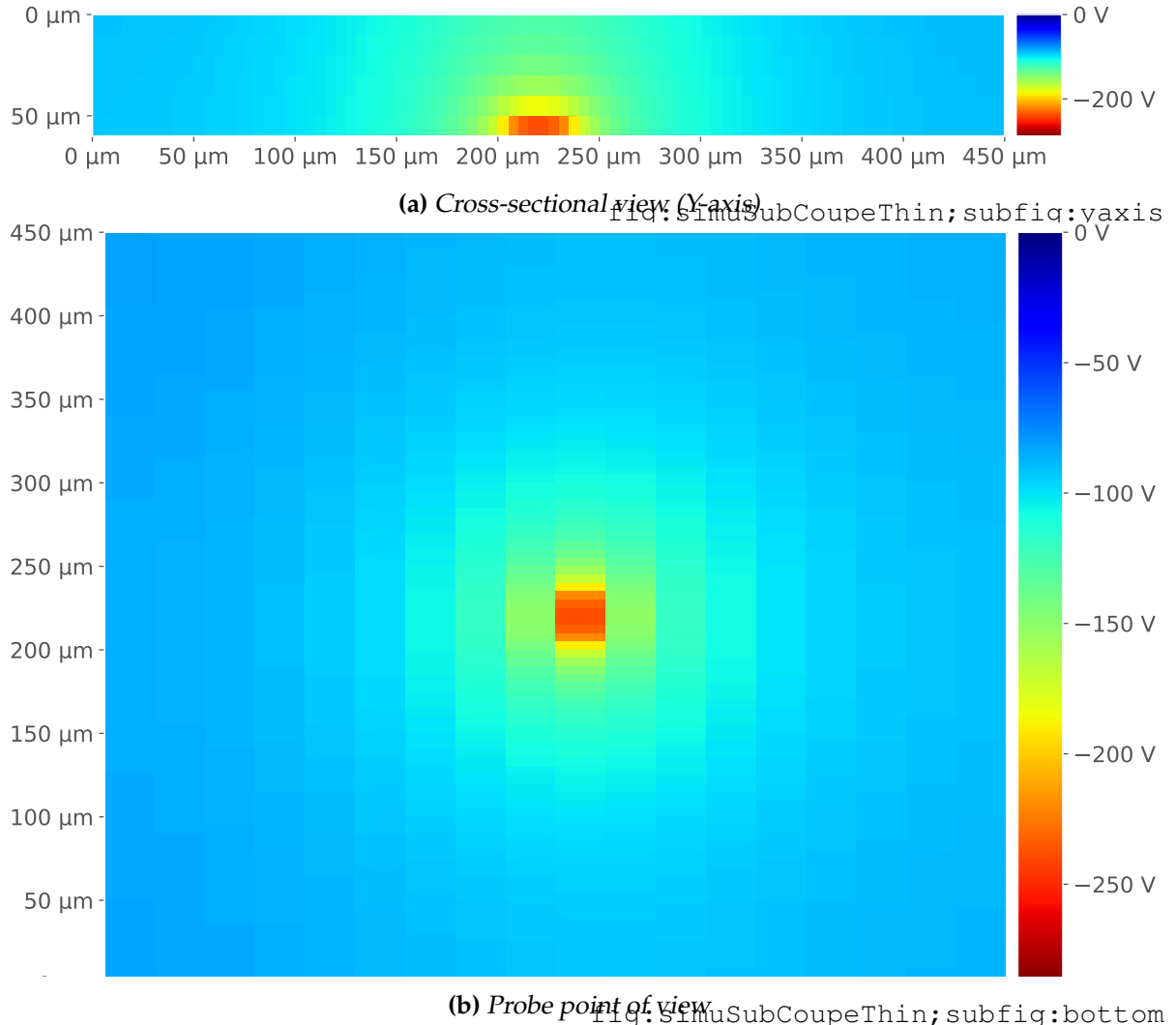


Figure 4.3: Simulated thinned IC (60 μm) substrate voltage distribution: peak of the first voltage pulse edge
 fig:simuSubCoupeThin

As stated previously, in order to verify the meaningfulness of the geometrical approach, we will complete it with an electrical modeling approach. For this purpose, the models introduced in Chapter 3 are reused. The electrical approach consists in generating ICs with different substrate thicknesses and simulating them during BBI. The considered ICs are 550 μm wide and 450 μm deep. Two substrate thicknesses are analyzed, 60 μm and 140 μm . The simulation parameters are the following:

- Triple-well substrate
- Required voltage pulse: -300 V
- Required pulse width: 20 ns

- Required rise and fall times: 8 ns

Fig. 4.2 and Fig. 4.3 show, for each simulated IC, the voltage bias across the substrate through different point of view at the apex of the voltage pulse first edge. For simplicity, results are shown in two dimensions and from two point of views: a cross-sectional view and a bottom view. The first interesting thing to note is that, as predicted thanks to the geometric model and as shown in Fig. 4.2 and 4.3, equipotentials effectively form half-circles into the substrate (half-spheres in 3D). They can be first observed from the bottom, where the voltage is spreading across the backside surface of the IC. Second, in the cross-sectional view, as it was illustrated previously with the geometrical model..... **IL Y A BEAUCOUP DE CHOSES À DIRE MAIS JE MANQUE D'INSPIRATION POUR CETTE PARTIE, JE REVIENDRAI PLUS TARD DESSUS.**

4.4 Models validation 2023-08-22 18:04:29+02:00

chap4:sect:modelValid

This section presents the conducted experiments allowing to validate the previously presented models.

4.4.1 IC substrate thinning quick look 2023-08-22 18:04:29+02:00

chap4:sect:modelValid:subsect:thinQuick

As substrate thinning is quite widespread when performing fault injection, let us have a quick look on how it is performed. Commonly, It is done using Selected Area Preparation (SAP) or Focused Ion Beams (FIB) milling. SAP milling consists in a very precise mechanical milling tool, generally able to remove material with a precision down to a few micrometers. However, it can often lead to uneven surfaces. FIB milling consists in a physical milling which does not imply a mechanical contact with the material to be removed, and allows nanometer-level precision. For that purpose, FIB is commonly used in combination with SAP [19] to produce even substrate surfaces. In addition to substrate thinning, SAP milling machines allow removing the plastic package and eventual internal metallic heat-sinks of ICs prior to substrate thinning. It has the advantage of providing low damage to thinned ICs, thanks to low spindle speed and low

temperature rise compared to traditional high speed milling.

4.4.2 Experiments with thinned circuits 2023-08-22 18:04:29+02:00

chap4 : sect : modelValid : subsect : XPthinning

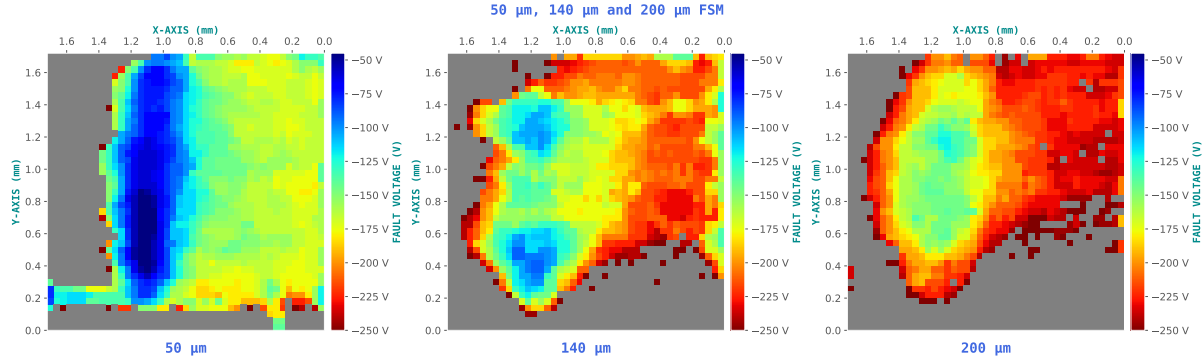


Figure 4.4: Fault susceptibility maps

fig:fsm1

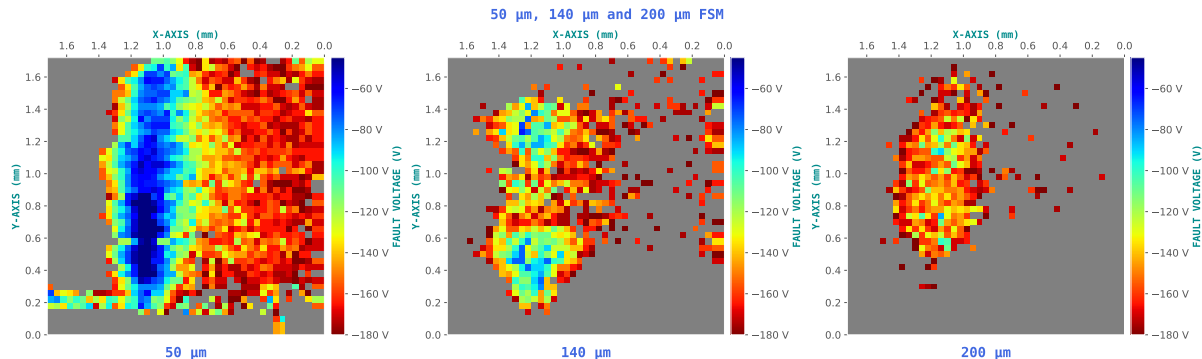


Figure 4.5: Susceptibility area spreading

fig:fsm1spread

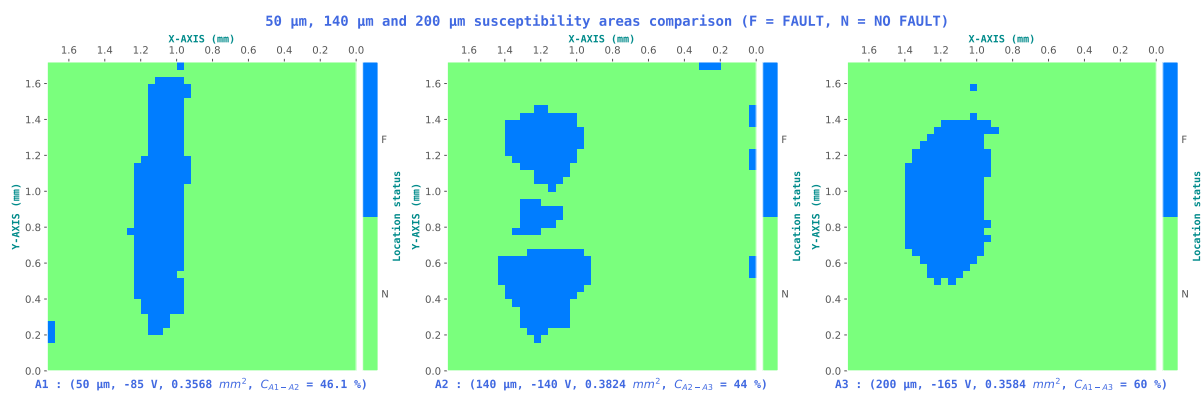


Figure 4.6: Fault susceptibility maps couples

fig:fsm1couple

With geometric and electrical modeling complete, it is now possible to conduct actual experiments in order to verify the meaningfulness of the previous approaches. In this

context, three an STM32F439VIT6 LQFP100 identical targets were thinned to three different levels, from 750 μm to respectively 200 μm , 140 μm and 50 μm , respectively named ST200, ST140 and ST50 for the rest of this Chapter. In order to verify the three conclusions extracted from the modeling section, three experiments are conducted for each target.

The first experiment aims at measuring the minimal voltage pulse amplitude V_{PU}^{MIN} required to induce a faulty behavior on an IC performing computations. These experiments are called Fault Susceptibility Maps (FSM). They allow spotting the region where the IC is sensitive to BBI, no matter which type of induced fault. Therefore, when mapping an entire IC, it is common to spot various areas not directly involved in the targeted calculation, like the analog voltage regulator or the FLASH memory logic control logic not to cite them all. As a result, and because in a fault injection context the cryptographic core is very often targeted, it was decided to focus the maps above the STM32 AES core only. Fig. 4.4 presents the three performed FSM. From left to right, t_{SUB} goes from 50 μm , then to 140 μm , finally to 200 μm . As stated before, the maps are performed above the hardware AES core of the IC, temporally aiming the penultimate AES round. The scanned area measures 1.7 mm by 1.7 mm, with a displacement step of 40 μm between each point. V_{PU} was limited to the following range: [30 V ; 280 V], with 5 V steps and a negative polarity. The pulse width was fixed at 6 ns. The first important thing to note here is that, as predicted with the geometric and electrical modelings, a thinner substrate allows a lower fault induction threshold. It is mainly shown thanks to the measurement of the average voltage required to induce a fault across the entire map, annotated at the top of each map. All of this sustains the first conclusion made in section 4.3.

Then, the second experiment, whose results are shown in Fig. 4.5, consist in analyzing the spreading of the BBI susceptibility area. The core of the experiment is identical as before. However, in order to highlight the spreading effect, it was required to set a lower maximum voltage amplitude (in absolute value). The value of 180 V was chosen as it is the average voltage of the medium-thinned IC. What is interesting here is that, for the ST200 target, because the voltage at the epitaxy level cannot reach the threshold value V_F in most cases, the fault area is tiny compared to the other targets, and focused

on the AES core. Then, concerning the ST140 target, thanks to the thinner substrate, the voltage at the epitaxy level can reach a higher value, and thus can cause more logic gates or further logic gates from the probe to have a faulty behavior. Eventually, the ST50 target shows the largest fault area. These experiments help to sustain the second conclusion of section 4.3.

Eventually, the last experiment consisted in finding, whenever possible, (t_{SUB}, V_{PU}) couples for which the susceptibility area is identical across all targets. The search for the couples of values was done by first choosing an arbitrary couple for ST200 target, and then calculating the correlation for each couple between the other two susceptibility areas and finding the highest correlation. Then, to confront the geometric modeling predictions, we calculated, thanks to equation 4.4, couples corresponding to

4.5 Conclusion 2023-08-22 18:04:29+02:00

This chapter introduced the interest of thinning the substrate of integrated circuits on Body Biasing Injection efficiency. In the first place, we studied thanks to a geometrical approach the potential benefits of this practice, further completed with electrical simulations. The geometric approach brought mathematical relations allowing to evaluate preliminary the effects of thinning the substrate of a target IC.

À FINIR.

V

Fault model 2023-08-22 18:04:29+02:00

chap:5faultModel

Contents

5.1	Summary <small>2023-08-22 18:04:19+02:00</small>	56
5.2	Introduction <small>2023-08-22 18:04:19+02:00</small>	56
5.3	Charge extortion <small>2023-08-22 18:04:19+02:00</small>	57
5.3.1	Sequential logic operation and simple fault model <small>2023-08-22 18:04:19+02:00</small>	57
5.3.2	Charge extortion <small>2023-08-22 18:04:19+02:00</small>	58
5.4	Silicon substrate charges propagation <small>2023-08-22 18:04:19+02:00</small>	58
5.5	Logic gates simulation under BBI <small>2023-08-22 18:04:19+02:00</small>	58

5.1 Summary 2023-08-22 18:04:29+02:00

chap5:sect:summary

In this chapter, we present a fault model for BBI. The objective of this chapter is to provide an explanation of the mechanisms and causes of faults in integrated circuits that are subjected to body biasing injection. The chapter3 electrical models can be used to explain how electrical charge displacement in the IC during a BBI pulse allows changing some logic gate output values. Therefore, it is possible to target a critical time in the IC calculation thanks to the ability to finely control the induced disturbances. Eventually, to verify the correctness of the proposed analysis, both substrate charge propagation and logic gate behavior studies will be conducted.

5.2 Introduction 2023-08-22 18:04:29+02:00

chap5:sect:intro

To further complete the understanding of BBI, in addition to having a reliable model to predict IC behavior, it is of great importance of having a precise fault model, in order to be able to set up countermeasures. Indeed, the main objective of studying fault injection techniques is to protect further secured ICs in order to consider during the design of new ICs, the implications of such countermeasures. As it has been said in Chapter 3, simulating at a transistor level an entire IC is unrealistic computationally speaking. Therefore, and because the previous models do not represent the logical functions of the considered ICs, we propose an additional step to the simulation workflow proposed in Chapter 3. This addition consists in extracting the propagated disturbances from standard-cell segments models, and injecting them into functioning logic gates. Thus, it allows appreciating logic gates behavior under BBI in order to get a deeper and more precise understanding of both electrical and functional fault creation mechanisms.

5.3 Charge extortion 2023-08-22 18:04:29+02:00

chap5:sect:chargeExtortion

This section explains the charge extortion mechanism at work during BBI which allows fault creation. The voltage pulse generator, at each edge of its pulse, injects and then extorts electrical charges into and out of the IC.

5.3.1 Sequential logic operation and simple fault model 2023-08-22 18:04:29+02:00

chap5:sect:chargeExtortion:subsect:seqLogic

As sequential logic is ubiquitous in contemporary integrated circuits, we shall examine its fundamental workings in greater detail. Sequential logic relies on a core element: the edge-triggered D flip-flop (DFF). They are a memory component that is governed by a clock. At each rising-edge or falling-edge (depending on the design) of the clock, DFFs sample their input and replicate it at their output. Between DFFs are placed the logic gates, which fulfill a specific logical function. Because of this, values in sequential logic circuits can only be changed at the clock edges. Hence, in the event that an adversary is able to alter a logical value for an extended period of time at the input of a DFF, the subsequent combinatorial logic will yield an incorrect value, which will propagate to the subsequent DFFs.

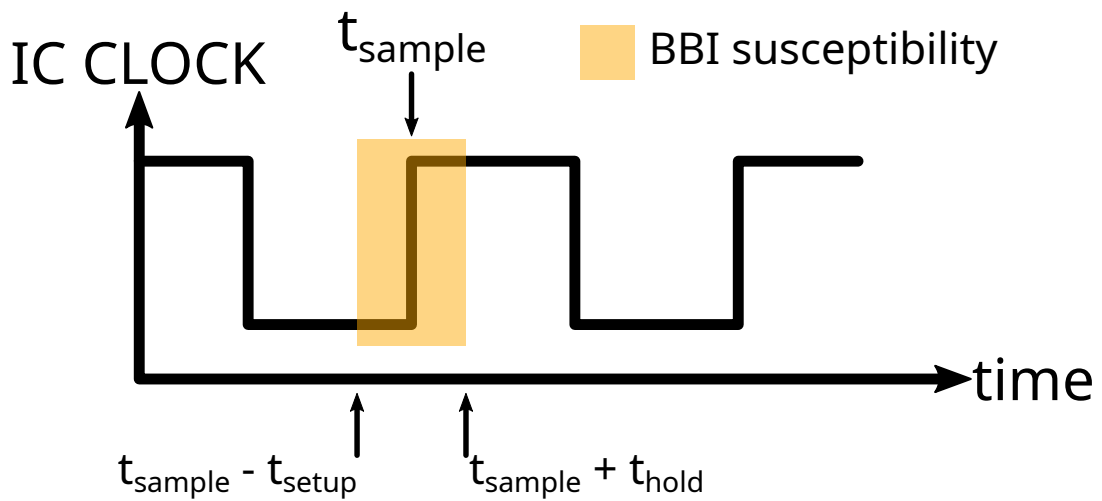


Figure 5.1: Sequential logic operation and BBI sampling fault susceptibility_{chap5:fig:bbiSusc}

This fault model we described previously is depicted in Fig. 5.1 and was first introduced in [20] for EMFI.

5.3.2 Charge extortion 2023-08-22 18:04:29+02:00

chap5:sect:chargeExtortion:subsect:chargeExtortion

5.4 Silicon substrate charges propagation 2023-08-22 18:04:29+02:00

chap5:sect:subEpiCurr

5.5 Logic gates simulation under BBI 2023-08-22 18:04:29+02:00

chap5:sect:simuLogic

VI

Conclusion

chap:6conclusion

Bibliography

- [1] G. Chancel, J.-M. Galliere, and P. Maurine. Body biasing injection: To thin or not to thin the substrate? In Josep Balasch and Colin O’Flynn, editors, *Constructive Side-Channel Analysis and Secure Design*, pages 125–139, Cham, 2022. Springer International Publishing. xvii, 26
- [2] Prasanna Ravi, Zakaria Najm, Shivam Bhasin, Mustafa Khairallah, Sourav Sen Gupta, and Anupam Chattopadhyay. Security is an architectural design constraint. *Microprocessors and Microsystems*, 68:17–27, 2019. 2
- [3] Paul C. Kocher. Timing attacks on implementations of diffie-hellman, rsa, dss, and other systems. In Neal Koblitz, editor, *Advances in Cryptology — CRYPTO ’96*, pages 104–113, Berlin, Heidelberg, 1996. Springer Berlin Heidelberg. 6
- [4] A. Shamir R.L. Rivest and L.Adleman. A method for obtaining digital signatures and public-key cryptosystems. In *Communications of the ACM*, volume 21, pages 120–126, 1978. 6
- [5] Boris Köpf and Markus Dürmuth. A provably secure and efficient countermeasure against timing attacks. In *2009 22nd IEEE Computer Security Foundations Symposium*, pages 324–335, 2009. 6
- [6] Paul Kocher, Joshua Jaffe, and Benjamin Jun. Differential power analysis. In Michael Wiener, editor, *Advances in Cryptology — CRYPTO’ 99*, pages 388–397, Berlin, Heidelberg, 1999. Springer Berlin Heidelberg. 6
- [7] Eric Brier, Christophe Clavier, and Francis Olivier. Correlation power analysis with a leakage model. In Marc Joye and Jean-Jacques Quisquater, editors, *Crypto-*

- graphic Hardware and Embedded Systems - CHES 2004*, pages 16–29, Berlin, Heidelberg, 2004. Springer Berlin Heidelberg. 7
- [8] Vincent Carlier, Hervé Chabanne, Emmanuelle Dottax, and Hervé Pelletier. Electromagnetic side channels of an fpga implementation of aes. *Cryptology ePrint Archive*, Paper 2004/145, 2004. <https://eprint.iacr.org/2004/145>. 7
- [9] J. Toulemont, G. Chancel, J. M. Galliere, F. Mailly, P. Nouet, and P. Maurine. On the scaling of emfi probes. In *2021 Workshop on Fault Detection and Tolerance in Cryptography (FDTC)*, pages 67–73, 2021.
- [10] Christophe Giraud. Dfa on aes. *Cryptology ePrint Archive*, Paper 2003/008, 2003. 20, 22
- [11] G. Chancel, Jean-Marc Gallière, and P. Maurine. Body biasing injection: Impact of substrate types on the induced disturbancesf. In *2022 Workshop on Fault Detection and Tolerance in Cryptography (FDTC)*, pages 50–60, 2022. 26
- [12] Mathieu Dumont, Philippe Maurine, and Mathieu Lisart. Modeling of electromagnetic fault injection. In *2019 12th International Workshop on the Electromagnetic Compatibility of Integrated Circuits (EMC Compo)*, pages 246–248, 2019. 26
- [13] M. Lisart M. Dumont and P. Maurine. Modeling and simulating electromagnetic fault injection. *IEEE Transactions on Computer-Aided Design of Integrated Circuits and Systems*, 40(4):680–693, 2021. 26, 27, 29
- [14] Yasuhiro Ogasahara, Masanori Hashimoto, Toshiki Kanamoto, and Takao Onoye. Supply noise suppression by triple-well structure. *IEEE Transactions on Very Large Scale Integration (VLSI) Systems*, 21(4):781–785, 2013. 31
- [15] Takuya Wadatsumi, Kohei Kawai, Rikuu Hasegawa, Takuji Miki, Makoto Nagata, Kikuo Muramatsu, Hiromu Hasegawa, Takuya Sawada, Takahito Fukushima, and Hisashi Kondo. Voltage surges by backside esd impacts on ic chip in flip chip packaging. In *2022 IEEE International Reliability Physics Symposium (IRPS)*, pages P14–1–P14–6, 2022. 37

- [16] Takuya Wadatsumi, Kohei Kawai, Rikuu Hasegawa, Kazuki Monta, Takuji Miki, and Makoto Nagata. Characterization of backside esd impacts on integrated circuits. In *2023 IEEE International Reliability Physics Symposium (IRPS)*, pages 1–6, 2023. 37
- [17] Breier et al. Extensive laser fault injection profiling of 65 nm fpga. *J Hardw Syst Secur* 1, pages 237–251, 2017. 44
- [18] Jakub Breier and Chien-Ning Chen. On determining optimal parameters for testing devices against laser fault attacks. In *2016 International Symposium on Integrated Circuits (ISIC)*, pages 1–4, 2016. 44
- [19] C. Boit, R. Schlangen, A. Glowacki, U. Kindereit, T. Kiyan, U. Kerst, T. Lundquist, S. Kasapi, and H. Suzuki. Physical ic debug and - backside approach and nanoscale challenge. *Advances in Radio Science*, 6:265–272, 2008. 51
- [20] S. Ordas, L. Guillaume-Sage, and P. Maurine. Electromagnetic fault injection: the curse of flip-flops. *Journal of Cryptographic Engineering*, 7(3):183–197, Sep 2017. 57